Cyclophane Molecules Exhibiting Thermally Activated Delayed Fluorescence: Linking Donor Units to Influence Molecular Conformation

Matthias Hempe,[a] † Alastair K. Harrison,[b] † Jonathan S. Ward,[a] † Andrei S. Batsanov,[a] Mark A. Fox,[a] Fernando B. Dias,*[b] and Martin R. Bryce*[a]

†These authors contributed equally to this manuscript.

[a] Chemistry Department, Durham University, South Road, Durham, DH1 3LE, UK
E-Mail: m.r.bryce@durham.ac.uk
[b] Physics Department, Durham University, South Road, Durham, DH1 3LE, UK
E-Mail: f.m.b.dias@durham.ac.uk

Abstract

The synthetic methodology to covalently link donors to form cyclophane-based thermally activated delayed fluorescence (TADF) molecules is presented. These are the first reported examples of TADF cyclophanes with 'electronically innocent' bridges between the donor units. Using a phenothiazine-dibenzothiophene-*S*,*S*-dioxide donor–acceptor–donor (D–A–D) system, the two phenothiazine (PTZ) donor units were linked by three different strategies: (i) ester condensation, (ii) ether synthesis, and (iii) ring closing metathesis. Detailed X-ray crystallographic, photophysical and computational analysis shows that the cyclophane molecular architecture alters the conformational distribution of the PTZ units, while retaining a certain degree of rotational freedom of the intersegmental D–A axes that is crucial for efficient TADF. Despite their different structures, the cyclophanes and their non-bridged precursors have similar photophysical properties since they emit through similar excited states resulting from the presence of the equatorial conformation of their PTZ donor segments. In particular, the axial-axial conformations, known to be detrimental to the TADF process, are suppressed by linking the PTZ units to form a cyclophane. The work establishes a versatile linking strategy that could be used in further functionalization while retaining the excellent photophysical properties of the parent D–A–D system.

Introduction

The concept of mechanically tethering molecular segments in materials chemistry has led to a broad variety of macrocyclic structures (e.g. cyclophanes,[1-5] catenanes,[6,7] rotaxanes[8-10]) in which intramolecular movements can be controlled to influence the resulting material properties and functions.[11]

Intramolecular motions and segmental orientations can have a strong impact on the properties of light-emitting organic materials.[12-14] State-of-the-art emitter molecules, which are based on the *thermally activated delayed fluorescence* (TADF) principle can exploit up to 100% of the excitons formed under optical or electrical excitation.[15-21] Here, triplet excited states are converted to singlet states through a

harvesting mechanism known as *reverse intersystem crossing* (RISC).[22-29] Molecules exhibiting TADF are generally comprised of donor (D) and acceptor (A) segments, which are electronically decoupled, inducing a high degree of twist between the D–A segments.[30] This results in the formation of intramolecular charge transfer (CT) states, which by interacting with energetically close or degenerate local excited (LE) states facilitate the spin-flip from triplet state to singlet state. Attempts to explain the efficiency of this interconversion mechanism solely by the energy gap between singlet and triplet states did not lead to a conclusive explanation, and second order (vibrational) coupling between the excited states has now been shown to be fundamental to this process.[31-33] Conformations of the molecular segments can severely alter the ladder of electronic states within the system. Breaking or extending the π-conjugation length by molecular distortions, thereby shifting excited state energy levels, can completely change the emission mechanism and efficiency.[32,34,35] Therefore, structural dynamic considerations of the molecular segments are important when designing high performance light-emitting organic molecules.

In this respect, it was reported that in a series of phenothiazine-based (PTZ) materials, the donor segments can adopt two different conformations, axial (ax) and equatorial (eq), with respect to the dibenzothiophene-*S*,*S*-dioxide ($DBTO_2$)[36] and other acceptor units such as DPTZ-$DBTO_2$ in **Figure 1**.[37-39] PTZ derivatives show a small energy barrier between these conformations in solution.[40] Different properties resulting from the different conformations can be observed when selected PTZ-based molecules are embedded in a rigid, solid-state matrix.[36] The equatorial (eq) arrangement of the donor segments gives well aligned ^{1}CT and ^{3}LE states, resulting in efficient triplet harvesting by RISC and strong emission by TADF. In contrast, the axial (ax) conformer of the donor segments results in higher energy CT states and often leads to materials with large singlet-triplet energy gaps (ΔE_{ST}). Axial conformers therefore favor *room temperature phosphorescence* (RTP) in rigid, nonpolar zeonex matrices, with negligible TADF contributions.[12,13]

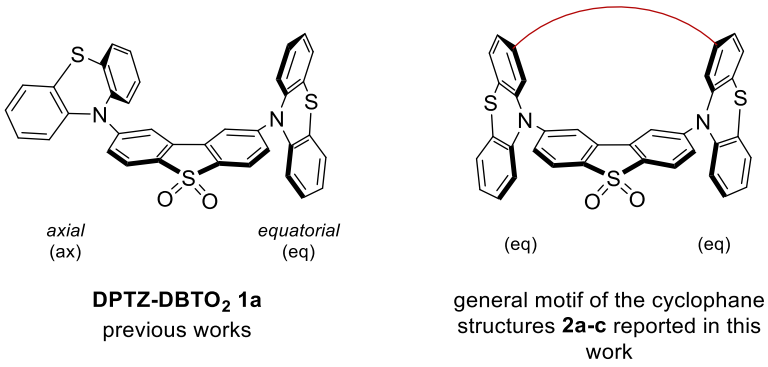

Figure 1. Schematic representation of the parent DPTZ-$DBTO_2$ donor-acceptor compound **1a** (left) and the respective cyclophanes **2a−c** of this work (right, red line represents a covalent link between the donor units).

Utilizing these distinct photophysical behaviors induced by conformational heterogeneity, a series of PTZ-$DBTO_2$ molecules with sterically demanding substituents at various positions was synthesized in previous works.[12,41] Methyl groups in the 1-position of the PTZ units reduce the conformational flexibility of the unsubstituted parent compound and predominantly lead to the axial arrangement of the donor segments within the materials, which strongly emit RTP in zeonex matrix. In contrast, introducing methyl and isopropyl substituents at the $DBTO_2$ acceptor site gives only equatorial arrangement of the donor units.[35] Substitution at the acceptor positions changes the emission mechanism to TADF without RTP.

Taking these insights into account, a series of TADF cyclophanes **2a−c** are herein presented, which reduce the conformational flexibility of the parent compound **1a** (**Figure 1**). Covalently tethering the donor segments into a macrocycle with an 'innocent' bridge leads to a new structural design of TADF molecules. This design differs from literature macrocyclic TADF molecules[14,42] where all parts of the macrocycle are involved in the photophysics, whereas here the linker can be described as 'innocent'. In other examples,[43,44] the cyclophane acts as a double covalent linker between donor and acceptor, whereas in the present work the two donors are tethered together to form the macrocycle. All-aliphatic cyclophanes have been 'bolted' on to 'remote sites' of TADF molecules as a substituent,[45] but the donor units have not been previously linked to form a cyclophane as presented herein. The macrocyclization was achieved through three different chemical linkages using either (i) ester formation, (ii) ether condensation, or (iii) alkene ring closing metathesis reaction. These modifications have introduced molecular handles of various polarity while retaining the excellent photophysical performance of the parent compound **1a**.

Results and discussion

Molecular design and synthesis

The syntheses of the cyclophanes were based on a derivatization approach of the key intermediate **1b**, which can be obtained in a six-step synthetic sequence starting from 2-cyanophenothiazine (**Scheme 1**). In the first step of this sequence, 2-cyanophenothiazine **3** was hydrolysed using a mixture of HCl and AcOH to obtain the corresponding carboxylic acid **4**. It was found that this reaction needs to be conducted in the absence of oxygen, since prior attempts in the presence of oxygen led to the formation of a chlorinated side-product (GC-MS analysis) which could not be separated from the resulting reaction mixture. Compound **4** was transformed into the methyl ester **5**, which was then reduced using $LiAlH_4$ to obtain the phenothiazine alcohol **6**. Here, it was observed that the reduction reaction of compound **5** proceeded with higher overall yield over two steps, than in the case of directly reducing the carboxylic acid **4** with $LiAlH_4$ to obtain the corresponding alcohol **6**. The benzyl alcohol **6** was protected using *tert*-butyldimethylsilyl chloride (TBDMS-Cl), and was subsequently used in a twofold Buchwald-Hartwig

cross-coupling reaction with 2,8-dibromodibenzothiophene-*S*,*S*-dioxide. Finally, the precursor molecule **1b** of the derivatization approach was obtained by deprotection of compound **8** using tetrabutylammonium fluoride (TBAF).

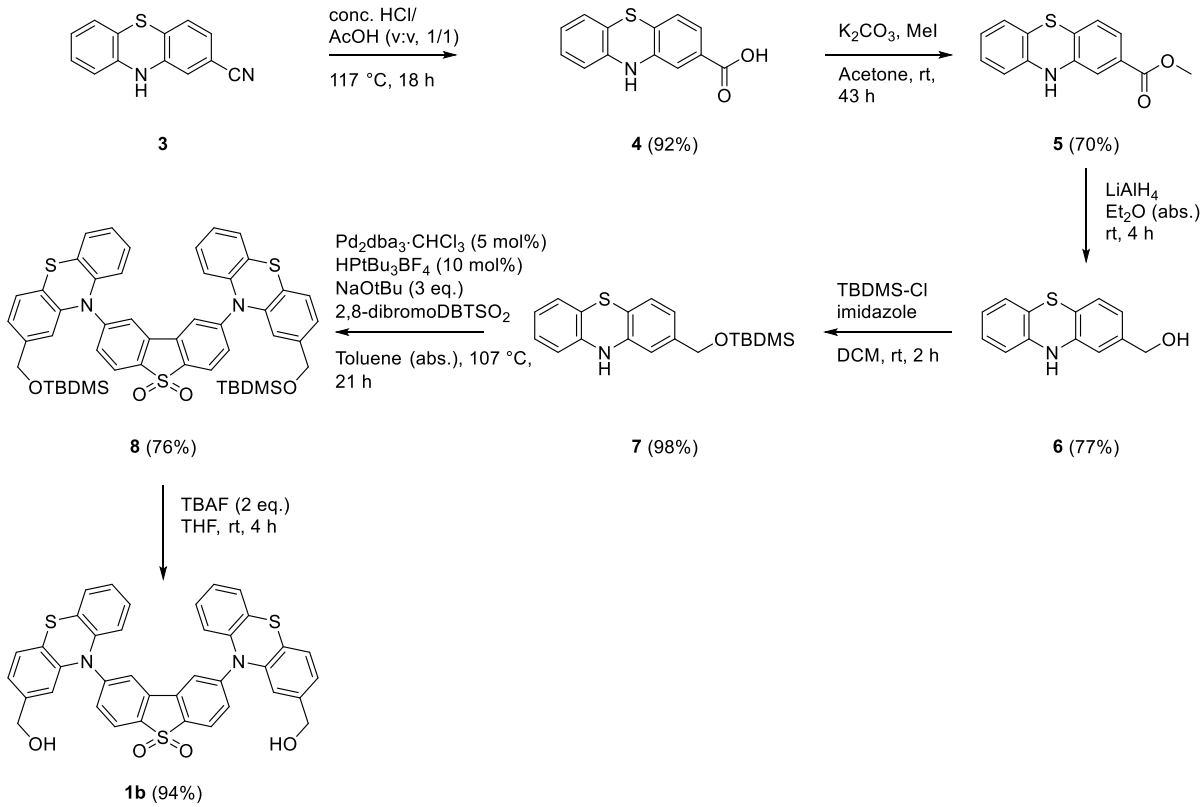

Scheme 1. Reaction sequence towards key intermediate **1b**.

The cyclophane ester structure **2a** was synthesized by the twofold esterification reaction of the diol **1b** with isophthaloyl chloride under high dilution, while the cyclophane ether **2b** was obtained by a twofold Williamson ether synthesis reaction using dibromo-*m*-xylene **10**. The synthesis of the alkene-based cyclophane **2c** followed a two-step reaction sequence. Initially, the diol **1b** was transformed into the bis-allyl substituted compound **1c**, which subsequently was converted into the cyclophane **2c** by a ring-closing metathesis (RCM) reaction. The *(E)*-configuration of the resulting alkene was confirmed by ^{1}H-NMR spectroscopy, as well as single crystal X-ray analysis.

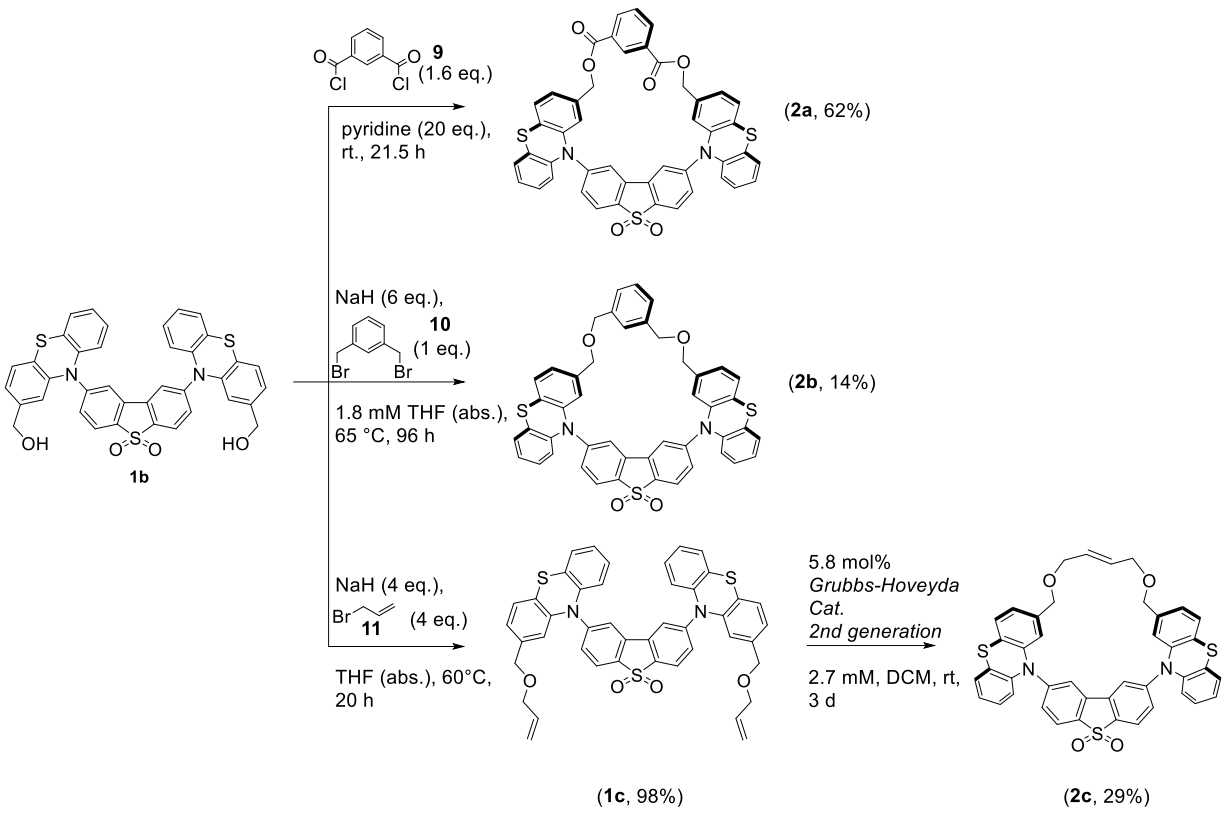

Scheme 2. Synthetic overview of the open derivative **1c** and the closed TADF cyclophane structures **2a–2c**.

X-Ray Crystallographic Analysis

The structures of the cyclophanes (**2a–c**) and the 'open' (non-bridged) disubstituted precursor compounds (**1b–c**) were determined by single crystal X-ray diffraction (**Figure 2**, **Table 1**). The asymmetric unit of **1b**·½Me_2CO comprises two molecules (*A* and *B*). In both, the PTZ units adopt *syn*-axial orientations with respect to the DBT plane and are folded outward along the N…S vectors by *ca.* 140°. The torsion angles (τ) about the N–C_{DBT} bonds are negligible and these bonds are shorter than the N–C_{PTZ}, i.e. the N lone pair is conjugated mainly with the acceptor unit. The intramolecular cavity in molecule *A* is filled by an acetone molecule of crystallization, which causes significant conformational changes: the transannular S…S distance (8.12 Å in *B* vs. 9.27 Å in *A*), the angle between N…S vectors (9.1° vs 31.4°), the interplanar angle between the inward-looking PTZ arene rings (61.4° vs 73.0°), and the S…N–C_{DBT} angles (**Table 1**) are all widened, the deviations (δ) of the N atoms from planarity are smaller and the N–C_{DBT} bonds are stronger in molecule *A*. All OH-groups form strong (O…O 2.659(3) to 2.804(3) Å) hydrogen bonds with one another: each molecule participates in two $R_4^4(8)$ rings[46] (**Figure S33b**), each ring involves OH-groups of molecules *A*, *B* and their equivalents generated by the glide plane, resulting in a continuous double-ribbon in the [1 0 1] direction. Remarkably, in molecule *A* both C–OH bonds are oriented roughly perpendicular to the PTZ arene planes, looking into its (wider)

transannular cavity, while in molecule *B*, both are nearly coplanar with their arenes. Thus, both molecules conform to the same (approximate) mirror plane passing through their SO_2 groups. The latter, as in other structures (*vide infra*), only accept weak C-H···O bonds. Molecule **1c** has crystallographic twofold (C_2) symmetry and the *anti*-axial orientation of the PTZ units. Several open D–A–D phenothiazine derivatives have been shown to exhibit the axial conformation as their minimum energy conformation by photophysical analysis and supporting DFT calculations.[13,47] Compared to **1b**, **1c** has more folded PTZ, wider S…N–C_{DBT} angles, more planarized N atoms and shorter N-C_{DBT} bonds (**Table 1**). Due to close intramolecular contacts between the (partly disordered) side-chains and the substituted PTZ arene rings, there is no intramolecular cavity and no solvent of crystallization in the structure of **1c**.

In contrast, cyclophanes **2a** (ester), **2b** (benzyl ether) and **2c** (allyl ether) all have an equatorial arrangement of both PTZ units, with near-perpendicular twists around the N–C_{DBT} bonds, near-linear S…N–C_{DBT} angles and less folded PTZ systems (**Table 1**). The N lone pair is conjugated with the PTZ, rather than DBT-*S*,*S*-dioxide, π-system, as indicated by the bond distances N-C_{DBT} > N-C_{PTZ}. The common features of all three cyclophane structures are a rigid intramolecular cavity which hosts a solvent molecule of crystallization, and intense disorder of the bridge, revealing their conformational flexibility (**Figures S35−S37**). In **2a**·1.5CH_2Cl_2, one PTZ unit and the entire bridge except one methylene group, are disordered between two conformations, with occupancies 0.729(4):0.271(4). The intramolecular cavity (and an adjacent intermolecular void) is filled with disordered CH_2Cl_2 of crystallization. In the structure of **2b**·Me_2CO there are two crystallographically non-equivalent host molecules, each enclosing an acetone molecule in its cavity. Both **2b** molecules (as well as the solvent molecules) possess crystallographic mirror symmetry and have the bridge disordered equally between two (overlapping) positions related by the mirror plane. In both **2a** and **2b**, the arene ring of the bridge is disordered between two coplanar positions. Molecule **2c** has no crystallographic symmetry; the central ethylene moiety of the bridge shows a pedal-motion type disorder in a 0.87(1):0.13(1) ratio. In **2a** and **2c**, the PTZ units are folded outward, and in both donor of **2b**, inward.

Table 1. Selected geometrical parameters

	1b, *A*	**1b**, *B*	**1c**	**2a**	**2b**	**2c**
PTZ fold, °	139.5 140.1	140.1 140.5	125.3	152.6 155.2	147.1, 158.8 150.6	157.6 159.3
S…N-C_{DBT}, °	113.9 120.2	100.0 106.7	125.5	171.7 173.1	166.4 169.1	173.1 173.6
τ(N-C_{DBT}), °	1.2, 0.7	4.1, 7.7	0.0	83.9, 89.9	82.2, 85.3	81.0, 87.7
δ(N), Å	0.19	0.30	0.08	0.17	0.16	0.11
N-C_{DBT}, Å	1.405(2)	1.418(2)	1.397(4)	1.441(4)	1.438(13)	1.446(6)
N-C_{PTZ}, Å	1.436(3)	1.436(3)	1.427(4)	1.417(4)	1.417(13)	1.420(6)

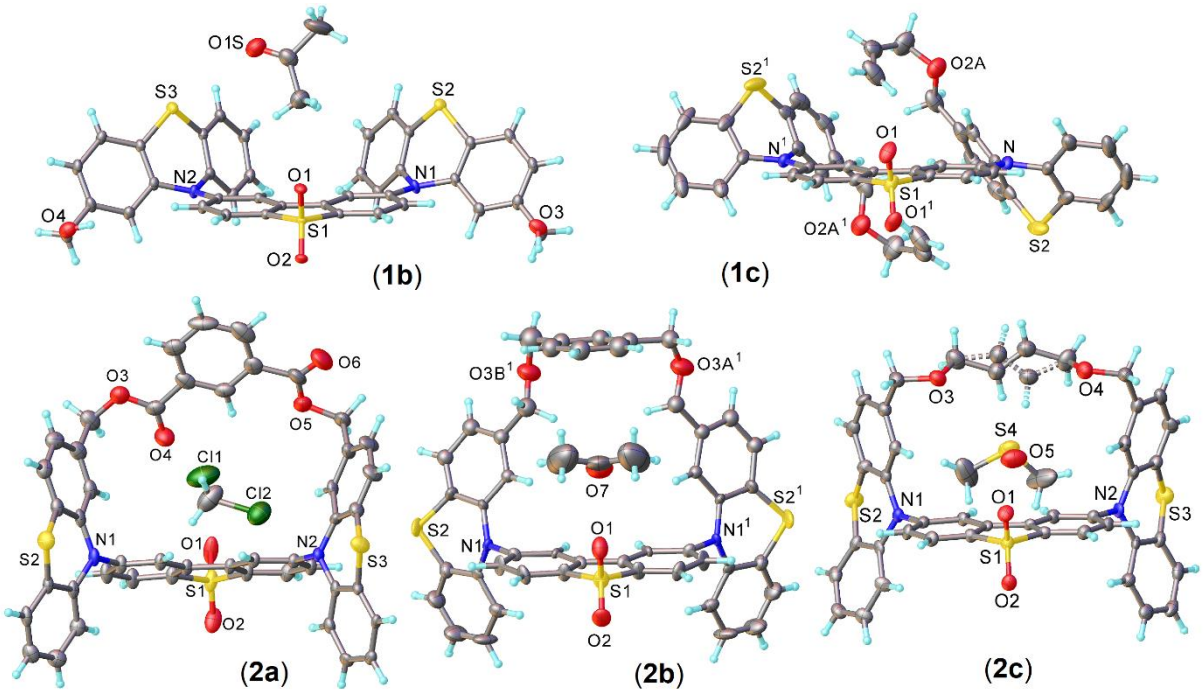

Figure 2. X-ray molecular structures of **1b–c** and **2a–c** with guest solvent molecules. Atomic displacement ellipsoids are drawn at the 50% probability level. Primed atoms are symmetrically related by 2-fold axis (**1c**) or mirror plane (**2b**). Disorder in **1c**, **2a** and **2b** is omitted (**Figures S34–36**).

Photophysical properties

Photophysics in Solution

Figure 3a shows the absorption spectra of open compounds **1b–c** and cyclophanes **2a–c** in DCM solution, together with the absorption of the individual D and A units (PTZ and $DBTO_2$ respectively) and the absorption of parent compound DPTZ-$DBTO_2$ **1a**,[32] used for comparison. Three main bands are observed which clearly match the absorption of the individual D and A units, indicating vestigial conjugation across the D and A fragments. This indicates that the phenothiazine donor units are electronically decoupled from the acceptor due to their highly twisted orientation relative to the plane of the acceptor unit (**Figure 2**). The bands peaking at 270 nm and 340 nm are mainly identified with the PTZ unit, whereas the band peaking at 290 nm is mostly due to the absorption of $DBTO_2$. Interestingly, the relative individual contributions of the D and A units to the absorption spectra changes between open (**1a–c**) and closed (**2a–c**) forms. In the molecules with open structures **1a–c**, the two bands peaking at longer wavelengths are more intense than in the closed forms **2a–c**. Similar trends have been observed previously in the absorption of related compounds, where the presence of mixed equatorial and axial conformers leads to the observation of absorption spectra similar to the spectra of compounds with open structures. In contrast compounds where the equatorial form dominates show absorption spectra that resemble the spectra of compounds with closed structures.[35] It is therefore suggested that compounds **1b** and **1c** with an open structure may adopt mixed equatorial/axial forms whereas compounds **2a−c** are

predominantly in an equatorial form in solution. This is consistent with similar electrochemical behavior of the materials which was investigated using cyclic voltammetry in DMF solution (**Table S1**). These data indicate the presence of the lower bandgap equatorial conformer in all open and closed derivatives of the set.

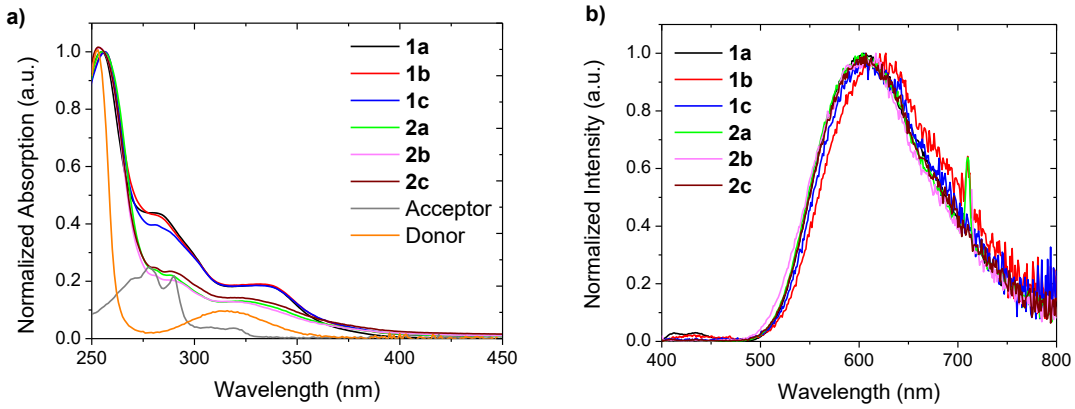

Figure 3. a) Normalized absorption spectra of the open compounds **1a–c** cyclophane structures **2a–c** and unsubstituted D and A units obtained in DCM at RT. b) Normalized emission spectra of **1a–c** and **2a–c** in toluene at RT (excited at 355 nm).

The emission of the D–A–D compounds in methylcyclohexane (MCH) is given in **Figure S20**. All compounds measured show red-shifted emission relative to the emission of the D and A single units. Moreover, the emission spectra in toluene (**Figure 3b**) are red-shifted compared in less polar MCH (see **Table 2** and **Figure S20**). This is consistent with the charge transfer (CT) character of the excited state in these compounds. However, no significant differences were observed among the emissions of the different compounds in toluene, and all compounds show pronounced solvatochromism when the spectra are collected in solvents of increasing polarity (**Figure S21**).

The luminescence of all the compounds **1a−c** and **2a−c** significantly increased in solution (**Table S3**) upon the removal of oxygen with no observable change in the profile of the spectra (**Figure S22**). This gives strong indication that the delayed fluorescence (DF) is a result of harvesting triplet states and is responsible for the increasing emission intensity in degassed samples.

The dependence of DF on the laser excitation dose was investigated in toluene. Compounds **1b−c** and **2a−c** all displayed a strong linear fit (gradient ≈ 1) of the DF integral as a function of power in a log-log plot (**Figure S23**) which is consistent with the reported data for **1a**.[32] This shows that the DF originates via an intramolecular mechanism, rather than bimolecular triplet-triplet annihilation (TTA) which would give a DF quadratic dependence with excitation dose. Introduction of the bridging unit between the two donor units in **2a−c** does not affect the emission mechanism, despite the different functionality on this bridge.

Time-resolved fluorescence decays of **1a−c** and **2a−c** were also measured in toluene. All the decays show two separate single-exponential regimes, with a fast component decaying in tens of nanoseconds, followed by a longer decay component in the sub-microsecond region (**Figure S24**). Molecule **1b** shows the fastest prompt fluorescence (PF) decay of only 12.1 ns although because the PLQY for **1b** is very low, some of the decay for this compound could drop below the sensitivity of the instrument. For the other derivatives, the PF decays were measured with a time constant of around 25 ns, consistent with the emission behavior observed for the parent compound **1a**.[32] The DF decay is also faster in molecule **1b**, with a time-constant of 485 ns, while the others show DF decays between 658 ns and 825 ns. The clear mono-exponential trend observed in the DF decay and the relatively similar decay constants, combined with the similar DF/PF ratios, suggests all these compounds are able to access the equatorial conformation in solution, as this conformation is known for exhibiting efficient TADF.[12,13] Due to a low energy barrier between axial and equatorial forms, interconversion between conformers is fully accessible for the open derivatives **1a−c**. This is consistent with previous observations in related compounds.[12,13] For the cyclophane structures **2a–c**, the equatorial arrangement of the PTZ segments is a result of the specific structural features of the molecules. Here, there is no significant effect of the polarity and rigidity of the bridging unit (aryl ester, benzyl ether, or allyl ether) on the emission properties. Therefore, in solution the intersegmental bridging of compounds **2a−c** appears to have no significant effect on the DF properties of these molecules. Using the solution data (**Table 2**) the RISC rate constant (k_{RISC}) is estimated to be $\approx 10^6\,s^{-1}$, with no significant variations among all molecules, including the parent compound **1a**.

Table 2. DF/PF ratio with prompt and delayed fluorescence lifetimes (in absence of oxygen) for all compounds in toluene.

Compound	Emission λ_{max} (nm) Toluene	MCH	DF/PF ratio	τ_{PF} (ns)	τ_{DF} (ns)	ϕ_{em} (%)[c]
1a	608	540[a]	2.05	31.8[a]	690[a]	10
1b	618	562	1.16	12.1± 0.5	484.8 ±24.8	4
1c	609	544	2.24	27.0± 2.3	787.1 ± 27.9	7
2a	601	571	2.24	27.2± 0.8	825 ± 21	7
2b	605	- [b]	1.47	25.4± 2.6	753 ± 37	7
2c	606	538	2.46	20.7± 2.7	658 ± 60	10

[a] Data from reference[35], [b] Data absent due to lack of solubility, [c] measured in the absence of oxygen

Photophysics in Solid State

The steady state emission spectra of compounds **1b–c** and **2a–c** in a solvent-free rigid matrix (zeonex film) are presented in **Figure 4**: all the compounds display blue-shifted emission maxima when compared to the measurements obtained in toluene solution. This shift is expected, due to the reduced polarity of zeonex compared to toluene. The emission of compounds **1c** and **2a–c** (**Figure 4**) peak

between 542 – 546 nm, **1a** peaks at 532 nm, while dihydroxy substituted compound **1b** is red shifted to 584 nm, maintaining an emission profile similar to that observed in solution. The zeonex films of **1b** also exhibited a cloudy white hue, suggesting the formation of aggregates large enough to scatter visible light. Films of **1b** were made at lower concentrations to reduce the effects of aggregation, however, despite reducing the concentration to 0.01 wt.% it was not possible to prevent aggregation. The phenomenon is likely to be due to the hydroxyl groups of **1b** raising the polarity significantly compared to the other molecules in the series. This increased polarity of the environment around the molecule red-shifts the charge transfer-based emission.

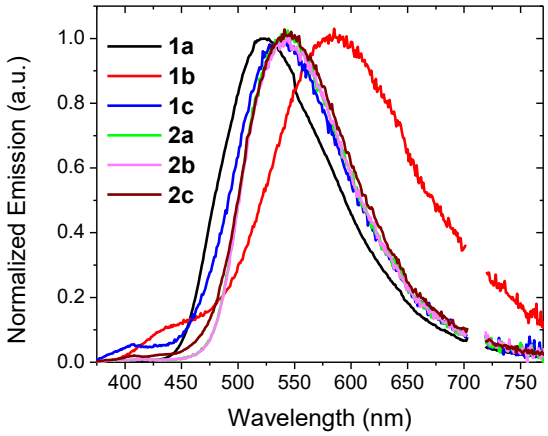

Figure 4. Normalized emission spectra of compounds **1a**–**c** and cyclophanes **2a**–**c** in zeonex (excited at 355 nm). A small section of the spectra was removed due to the second harmonic of the laser at 710 nm

The triplet harvesting properties of molecules **1a**−**c**, **2a**−**c** are also observed in zeonex films. Moderate dependence of the ^{1}CT fluorescence intensity on oxygen is observed for all compounds, suggesting triplet states are part of the pathway in the photophysical emission mechanism. However, when compared to the DF/PF ratio of **1a** in zeonex (**Table 3**), there appears to be no major macrocyclization effect on the photophysics, although subtle changes are observed. Upon degassing, a blue shift on the emission peak in zeonex is observed, up to 8–16 nm for the open structures **1a**−**c**, and only 2–4 nm for the closed structures **2a**−**c** (**Figure S25**). This shift in **1a** and was previously attributed to ^{3}LE phosphorescence.[12,13] The reduced blue-shift in the closed structures (**2a**−**c)** attributed to phosphorescence further suggests that the presence of axial PTZ conformers (which favor phosphorescence) is reduced by the cyclophane structure.

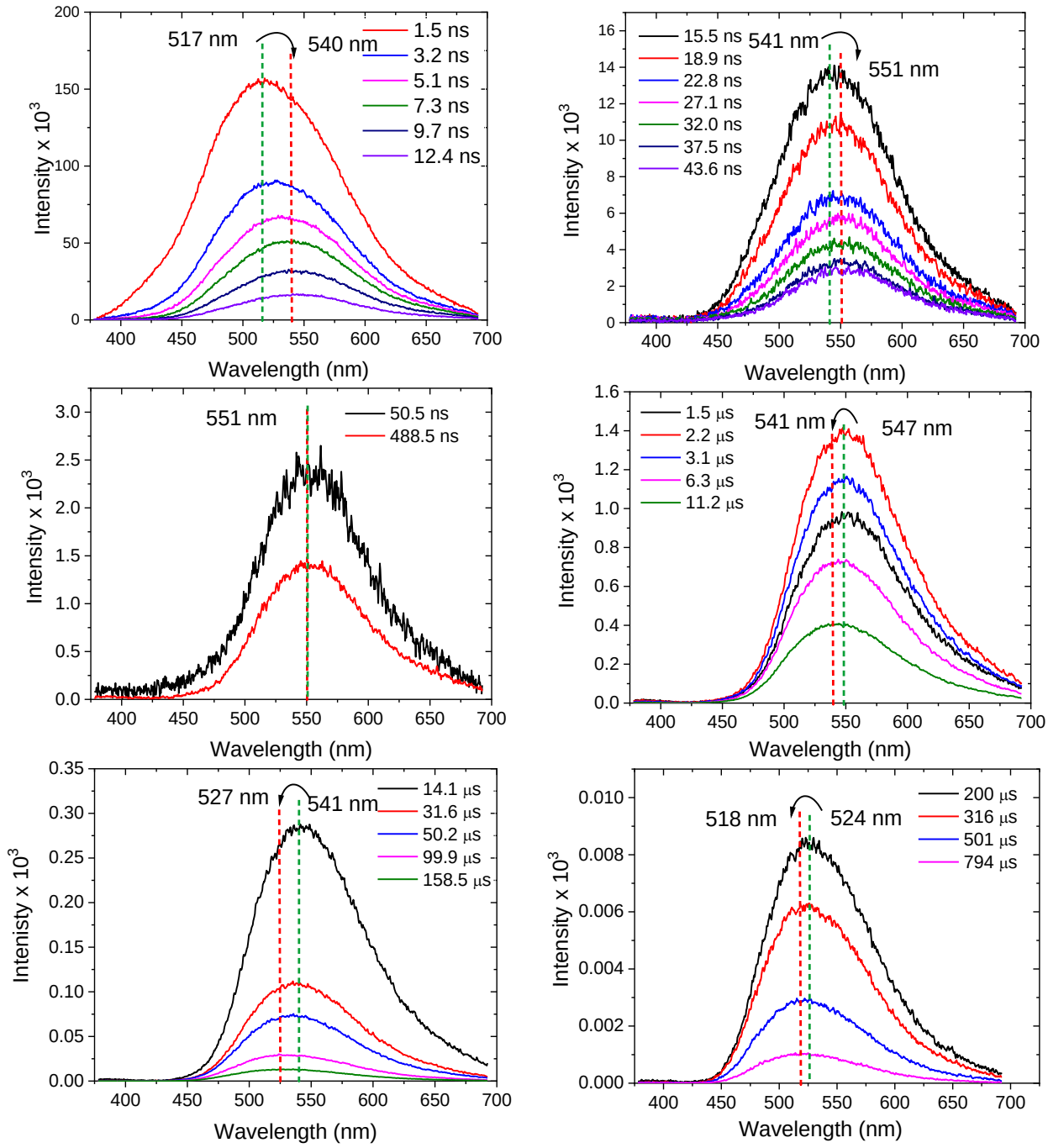

Figure 5. Time-resolved spectra obtained at different delay times for compound **2c** dispersed in zeonex at RT (excited at 355 nm).

Time-resolved emission spectra were measured for open compounds **1a–c** and cyclophanes **2a–c (Figures 5** and **S27–S31)** and **Figure 6** shows the relative shifts of the emission maxima for compounds **1a**, **1c** and **2a–c**. The initial emission maxima values at 1.5 ns correspond to a mixture of local and charge transfer fluorescence emissions. The local fluorescence emissions present at the 370–470 nm range in the steady state emission spectra, on the picosecond timescale (**Figures 5** and **S24**) are not recorded in the time-resolved measurements. The final emission maximum for **2c** at 518 nm (**Figure 5**)

is from room temperature phosphorescence (RTP) emissions. Charge transfer emissions (prompt and TADF) are those with the longest emission wavelengths in these time-resolved measurements. No apparent discernible pattern is observed between the two sets of compounds, with compounds **2a–c** (closed) and **1c** (open) displaying relative shifts in energy over the decay lifetime with a similar trend, however, with slightly smaller amplitude for the open structures. Therefore, we can conclude the analysis of temporal spectral shifts cannot in this case distinguish between open and closed structures. The analysis of the steady-state emission with and without oxygen is far more conclusive regarding the suppression of the axial conformer in the cyclophane structures **2a−c**.

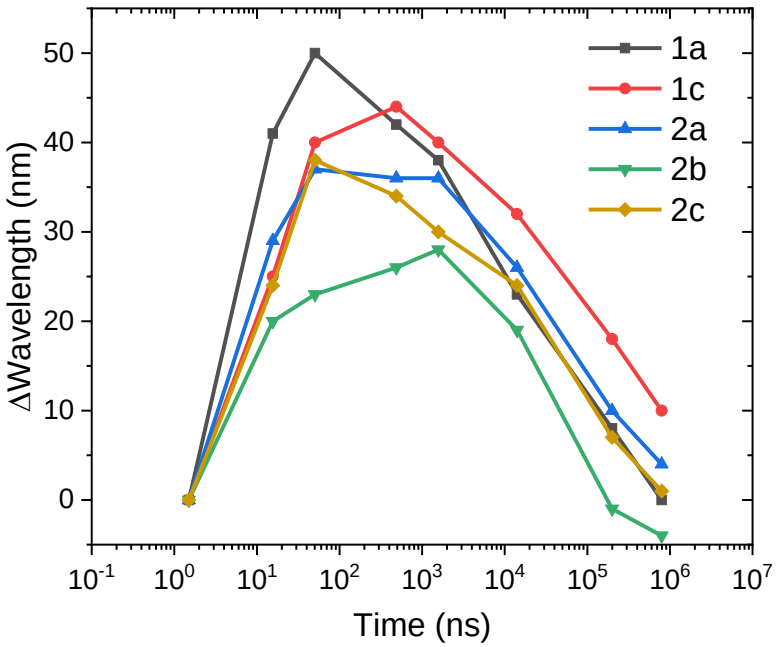

Figure 6. Relative shifts of the emission maxima over time for compounds **1a**, **1c** and cyclophanes **2a–c** in zeonex at RT. **1b** is omitted from this data as the low signal:noise ratio precludes accurate tracking of the wavelength.

Time dependent fluorescence decays were also recorded for **1b–c** and **2a–c** in zeonex (**Figure S26**). The decays were significantly more complex than those obtained in solution. This is due to multiple contributions from ^{1}LE states at early times, ^{3}LE phosphorescence and the presence of ^{1}CT fluorescence. Compounds **1b** and **2a–b** show very similar PF decays, around 9.0 ns, whereas compounds **1c** and **2c** give shorter PF lifetimes, around 5.0 ns. For the delayed fluorescence, compound **1b** shows a short DF lifetime of 1.1 μs and significantly lower PLQY, while compounds **1c** and **2a−c** have two exponential DF lifetimes of 2.0 μs - 4.7 μs for τ_1, and 18.6 μs to 30.8 μs for τ_2 (**Table 3**) indicating an overall slower RISC rate in the solid state compared to in toluene.

Table 3. Prompt and delayed emission lifetimes for all compounds in zeonex matrix.

Compound	DF/PF ratio	τ_{PF} (ns)	τ_{1DF} (μs)[a]	τ_{2DF} (μs)[a]	PLQY±5%[b]
1a	6.10	30.5	1.5	-	32%
1b	1.30	9.2	1.1	-	12%
1c	0.95	9.0	2.0	18.6	42%
2a	4.00	8.9	3.0	19.9	42%
2b	1.79	5.4	4.7	29.5	43%
2c	2.02	5.0	4.4	30.8	33%

[a] Shorter component of dual exponential fitting listed first as τ_1, longer component listed as τ_2
[b] Measured in the absence of oxygen

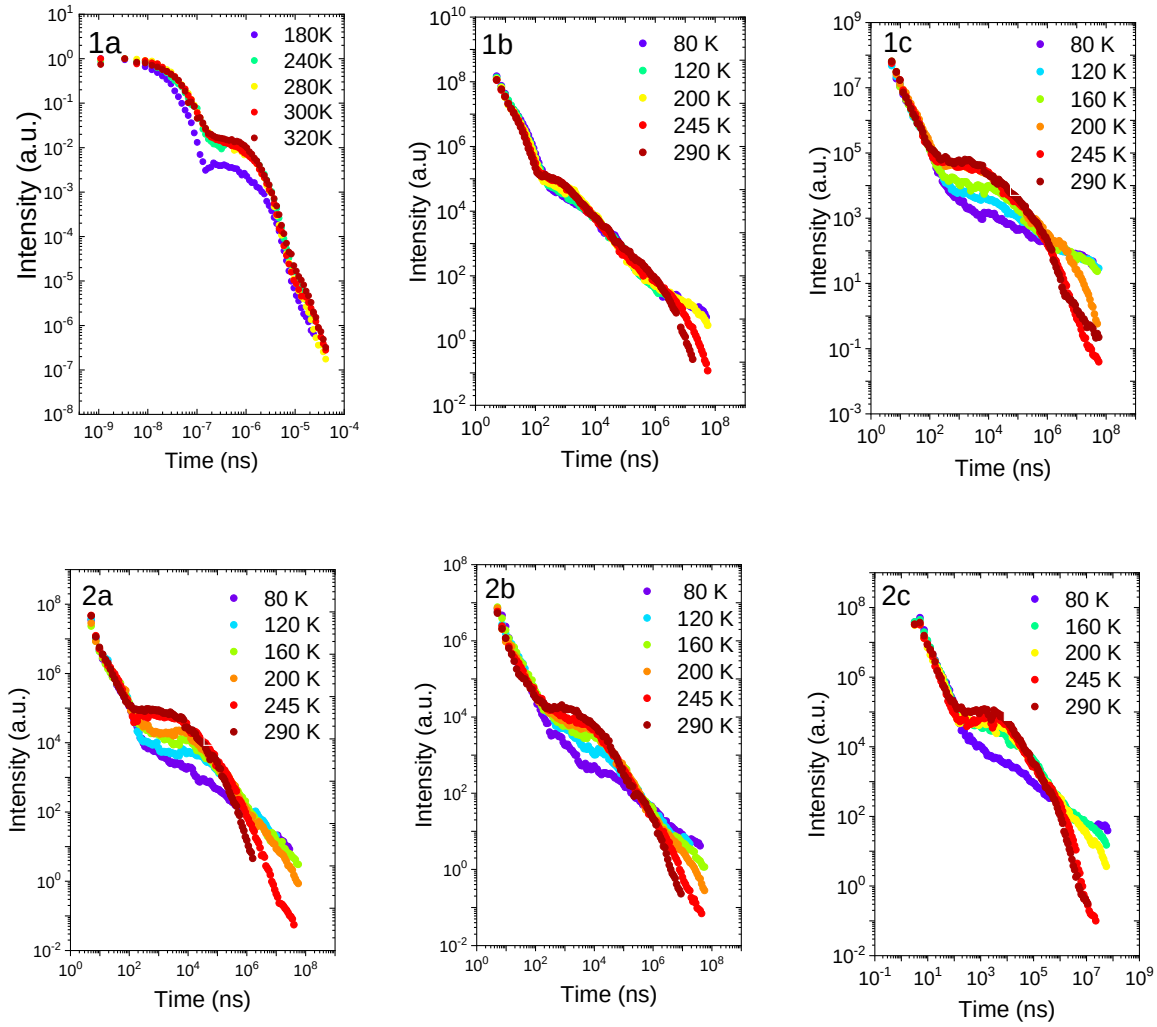

Figure 7. Temperature dependence of **1a−c** and **2a−c** in zeonex film.

Figure 7 shows the fluorescence decay curves for compounds **1a−c** and cyclophanes **2a−c** collected between 180 K and 320 K (for **1a**[32]) and between 80 K and 290 K (for **1b-c** and **2a-c**). No significant effect on the decay of PF is observed in the temperature range studied for all compounds. However, as expected, the delayed fluorescence shows marked temperature dependence. In all TADF compounds the DF is more intense at higher temperatures;[16] the exception in the present series is compound **1b** which

shows little DF contribution. This is expected due to the low PLQY, suggesting that the triplet excited state in **1b** is more affected by the non-radiative decay at longer lifetimes. In compounds **1c** and **2a−c** there is a significant change in intensity with an increase in temperature; this is additional evidence that the DF originates from a thermally activated mechanism (TADF). In compounds **2a** and **2b**, there is little (or no) change in DF intensity above 245 K, suggesting a small ΔE_{ST} barrier. In all compounds **1a−1c** and **2a−2c** phosphorescence is observed at low temperatures appearing as a longer decay component in the ms time range.

Computations

Detailed hybrid density functional theory (DFT) and time dependent DFT (TD-DFT) computations were performed on all six compounds **1a**–**c** and **2a**–**c** to support the interpretations of their photophysical data. The parent molecule **1a**, examined by hybrid-DFT in many studies elsewhere[12,13,32,48] shows that the seven distinct conformers of **1a** in the ground states (S_0) are very close in energies with three major classes, axial-axial (ax-ax), axial-equatorial (ax-eq) and equatorial-equatorial (eq-eq) related to the donor–acceptor orientations: the most stable conformer in each class is shown in **Figure 8**. The relative Gibbs free energies for these conformers are presented in **Table 4** with an energy difference of only 0.03 eV between the three forms. It is important to note that crystal structures of ax-ax and eq-eq conformers for **1a** and rotational barriers of only 0.12 eV between ax and eq orientations have been reported.[12,48] Thus all these conformers are expected to be present in solutions of **1a** and may all exist in the solid state as powder forms and in films.

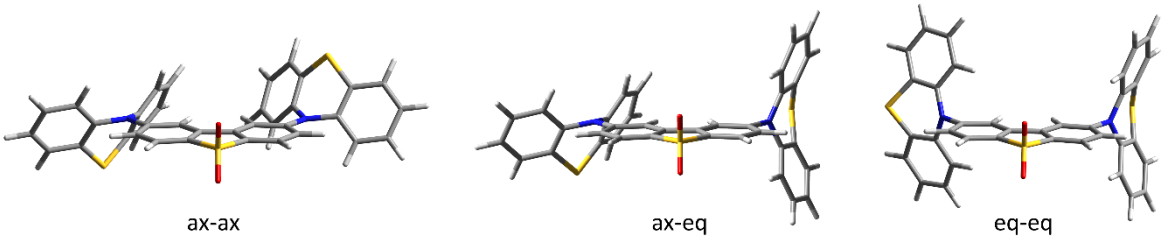

Figure 8. The lowest energy minima of the three main conformers, ax-ax, ax-eq and eq-eq, for **1a** at S_0 ground states.

Table 4. Relative Gibbs free energies (in eV) of most stable minima of ax-ax, ax-eq and eq-eq conformers of **1a-c** and **2a-c** at optimized S_0 ground states.

	ax-ax	ax-eq	eq-eq
1a	0.02	0.00	0.03
1b	0.00	0.03	0.01
1c	0.00	0.00	0.01
2a	0.76	0.07	0.00
2b	0.26	0.04	0.00
2c	0.17	0.11	0.00

Compounds **1b** and **1c** contain a substituent at each donor unit which resulted in 20 distinct conformers located from geometry optimizations based on the seven possible conformers of **1a** (**Figures S39**, **S40** and **S42**). The number of conformers multiplies further when the different orientations of the $–CH_2OR$ groups are also considered. There are favorable intramolecular hydrogen bond O-H…O interactions in **1b** which lower the energy by *ca.* 0.07 eV compared to conformers without such interactions. It is not surprising that **1b** has low solubility and issues of poor-quality film formation due to the discussed hydrogen bond interactions. The crystal structure of **1b** also contains intermolecular hydrogen bond interactions between two molecules. The relative energies of the most stable conformers of each class of **1b** and **1c** in **Table 4** are similar, thus all conformers are also expected to exist in solutions and in the solid state as powder forms and in films.

The three classes of ax-ax, ax-eq and eq-eq conformers for cyclophanes **2a**–**c** were also located with their relative energies listed in **Table 4** (**Figures S43–S45**). The bridges between the two donor units clearly result in the eq-eq conformers being the most stable of the three classes in contrast to **1a**–**c**, but the ax-eq conformers are only 0.04 (**2b**), 0.07 (**2c**) and 0.11 eV (**2a**) higher in energies. Such conformers may be present as minor components in solutions. The high relative energies of the ax-ax conformers rule out their presence in the conformational mixtures of the cyclophanes, **2a−c**.

Absorption spectra generated from ground states of the compounds in solutions show the distinct differences in the spectra of **1a**–**c** compared with **2a**–**c** are very likely due to the ax-ax conformers present in **1a**–**c** and the absence of ax-ax conformers in **2a**–**c** based on their relative energies (**Table 4**). The simulated absorption spectra for the three conformers (ax-ax, ax-eq and eq-eq) of **1a** and **2a** show bands present between 270 and 450 nm for ax-ax conformers (**Figure S38**). The predicted spectra are in accord with the absence of ax-ax conformers in the observed spectra for **2a-c** (**Figure 3**).

Unlike absorption spectra and optimized ground state geometries, emission spectra are from excited states and therefore are best modeled from optimized excited state geometries. The lowest singlet excited

state S_1 optimized geometries of **1a** at CAM-B3LYP/6-31G(d) were determined previously[12] for ax-ax and ax-eq conformers but not for eq-eq conformers. The phenothiazine remains folded in the ax orientation but becomes planar in the eq orientation at these optimized S_1 geometries. Here, all three most stable conformers of **1a** at S_1 states have very different relative energies with the eq-eq optimized geometry the most likely geometry in the excited state (**Table 5**, **Figure S46**). One phenothiazine unit is planar and the second phenothiazine unit is folded in the eq-eq optimized S_1 geometry. The ax-eq and ax-ax S_1 geometries at CAM-B3LYP/6-31G(d) are higher in energies than the eq-eq S_1 geometry by 0.24 eV and 0.81 eV, respectively. This energy pattern for the S_1 states of **1a** is repeated for the five new compounds **1b**–**c** and **2a**–**c** (**Table 5** and **Figures S47-S52**).

Table 5. Relative energies (in eV) of most stable minima of ax-ax, ax-eq and eq-eq conformers of **1a**–**c** and **2a-c** at optimized S_1 excited states.

	ax-ax	ax-eq	eq-eq
1a	0.81	0.24	0.00
1b	1.03	0.43	0.00
1c	0.80	0.23	0.00
2a	0.73	0.30	0.00
2b	0.75	0.20	0.00
2c	0.73	0.12	0.00

From the relative energies of the S_1 geometries in **Table 5**, it is not surprising to find that the observed emission data in toluene and zeonex for all six compounds are remarkably similar. The simple emission spectra in toluene along with TADF suggest all emissions are from the eq-eq S_1 excited state geometries. The complex emission spectra in zeonex with early prompt (local) fluorescence, charge-transfer/TADF and phosphorescence imply that more excited states are involved in these emissions due to constrained geometries in zeonex. It is noted elsewhere that crystals containing ax-ax conformers of **1a** give early prompt (local) fluorescence and phosphorescence emissions, whereas crystals containing eq-eq conformers of **1a** generate charge transfer/TADF emissions on excitation.[48]

Thermally activated delayed fluorescence (TADF) is considered to be present when the S_1 and T_1 energies are sufficiently close together to promote reverse intersystem crossing (RISC) along with favorable spin-orbit coupling (SOC) between the charge transfer (^{1}CT) singlet excited state and the local excitation (^{3}LE) triplet state when these states are close in energies. **Figures 9-10** and **S53**–**S55** show the excited states with natural transition orbitals (NTOs) involved in the TADF processes in **1a**–**c** and **2a**–**c** by TD-DFT computations. **Table 6** lists the nature and energies of these relevant excited states for

all six compounds where the nature of the excited states is similar in order, except for **1b**, and all states are relatively close in energies.

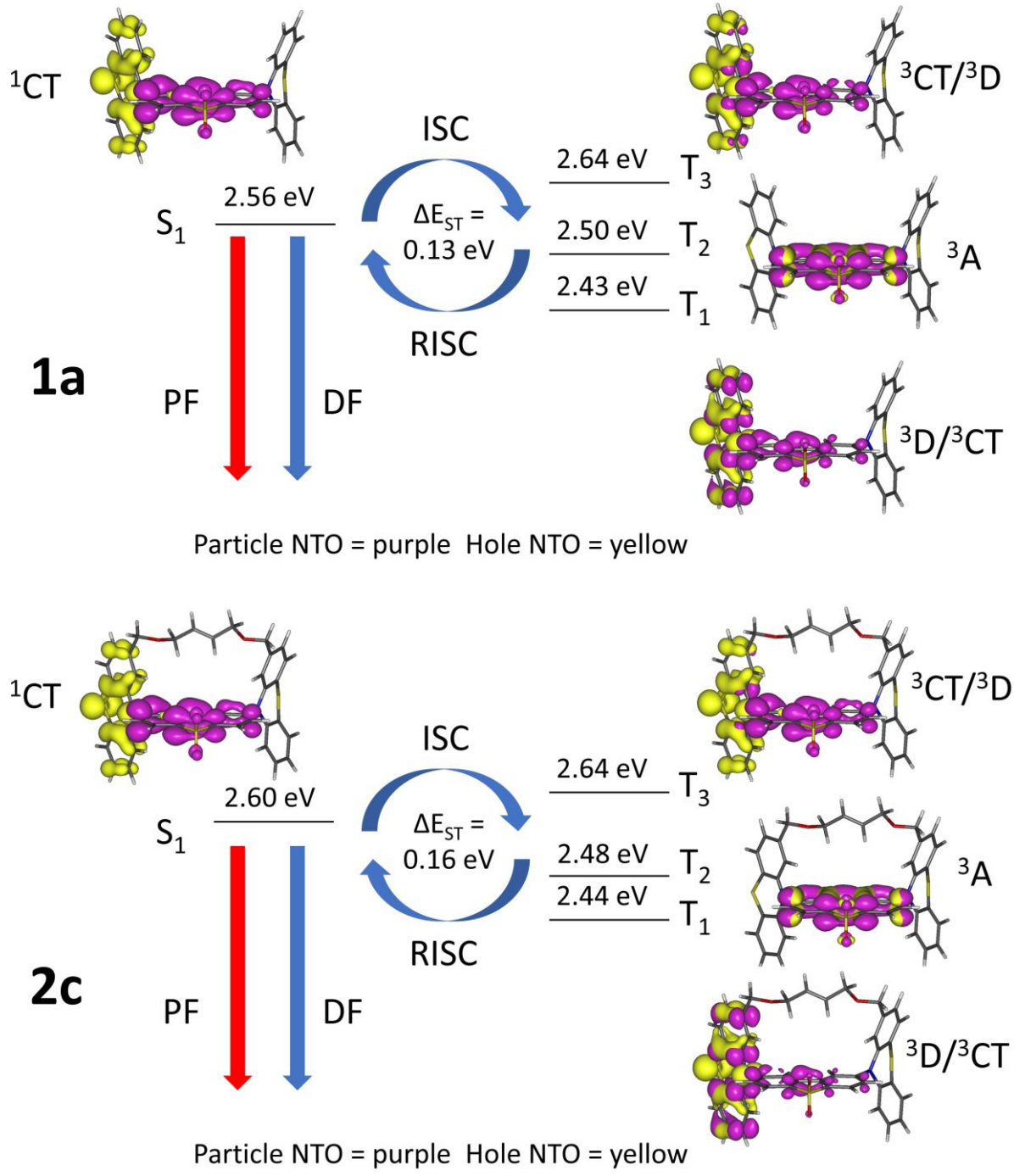

Figure 9. Energy diagrams illustrating TADF in **1a** and **2c** with natural transition orbitals (NTOs) for each state on optimized eq-eq S_1 excited state geometries from TD-DFT computations. PF = prompt fluorescence, DF = (thermally activated) delayed fluorescence, ISC = intersystem crossing, RISC = reverse intersystem crossing, ΔE_{ST} = S_1 energy – T_1 energy, ^{1}CT = singlet charge transfer state, ^{3}CT =

triplet charge transfer state, ^{3}D = local triplet excitation state at the donor unit, ^{3}A = local triplet excitation state at the acceptor unit. ^{3}D/^{3}CT and ^{3}CT/^{3}D are mixed states where the former state is dominant. Contours in NTOs are drawn at ±0.04 (e/bohr^3)$^{1/2}$.

Table 6. Energies and nature of the excited states from TD-DFT computations on optimized eq-eq S_1 geometries of **1a−c** and **2a−c**. %CT values are listed in parentheses. ΔE_{ST} = S_1 energy – T_1 energy and ΔE_{TT} = T_2 energy – T_1 energy.

	T_1 ^{3}D/^{3}CT	T_2 ^{3}A	S_1 ^{1}CT	T_3 ^{3}CT/^{3}D	ΔE_{ST}	ΔE_{TT}
1a	2.43 (47)	2.50 (11)	2.56 (97)	2.64 (59)	0.13	0.07
1b	2.28 (64)	2.45 (23)	2.34 (73)	2.53 (26)	0.06	0.17
1c	2.42 (40)	2.50 (10)	2.58 (97)	2.64 (67)	0.16	0.08
2a	2.40 (28)	2.49 (8)	2.50 (96)	2.60 (77)	0.10	0.09
2b	2.41 (58)	2.51 (18)	2.53 (97)	2.63 (56)	0.12	0.10
2c	2.44 (34)	2.48 (22)	2.60 (97)	2.64 (77)	0.16	0.04

The singlet states (S_1) in **1a**, **1c** and **2a−c** from the calculated NTOs have essentially pure charge transfer character (96–97%) which is expected from the pronounced solvatochromism observed in the emission spectra (**Figure S21**). The three lowest energy triplet states, T_1, T_2 and T_3, in all compounds do not include a pure charge transfer triplet state (^{3}CT). Mixtures between local donor (^{3}D) and charge transfer (^{3}CT) states are apparent in T_1 and T_3 states, whereas T_2 states are local acceptor (^{3}A) states. These local triplet states (^{3}LE) being close in energies (ΔE_{ST} 0.10–0.16 eV) with the S_1 charge transfer states facilitate TADF as spin orbit couplings (SOCs) with SOC matrix elements (SOCME) at 0.22–0.58 cm^{-1} occur between singlet and triplet states of different orbital characters (**Table S3**). Spin orbit couplings between a singlet charge transfer state and a triplet charge transfer state are formally forbidden (SOCME = 0.00 cm^{-1}). The vibronic couplings between close low energy triplet states (ΔE_{TT} 0.04–0.10 eV) are also assumed to aid the RISC process for TADF. The NTOs of the pertinent excited states in **2a**–**c** are located at the donor (phenothiazine, PTZ) and/or acceptor (dibenzothiophene-*S*,*S*-dioxide, $DBTO_2$) units so the linkers between the two PTZ units can be regarded as 'electronically innocent'.

The eq-eq S_1 optimized geometry for diol **1b** differs from other eq-eq S_1 geometries (**1a**, **1c** and **2a**–**c**) due to the intramolecular hydrogen bond interaction between two phenothiazine units, and thus the energies of the excited states and order of the nature of the triplet states in **1b** change somewhat from those in **1a**, **1c** and **2a**–**c** (**Figure 10**). The energy of the S_1 transition state is substantially lower compared to **1a**, **1c** and **2a−c** in accord with lower emission energies observed experimentally in **1b** compared to **1a**, **1c** and **2a**–**c**.

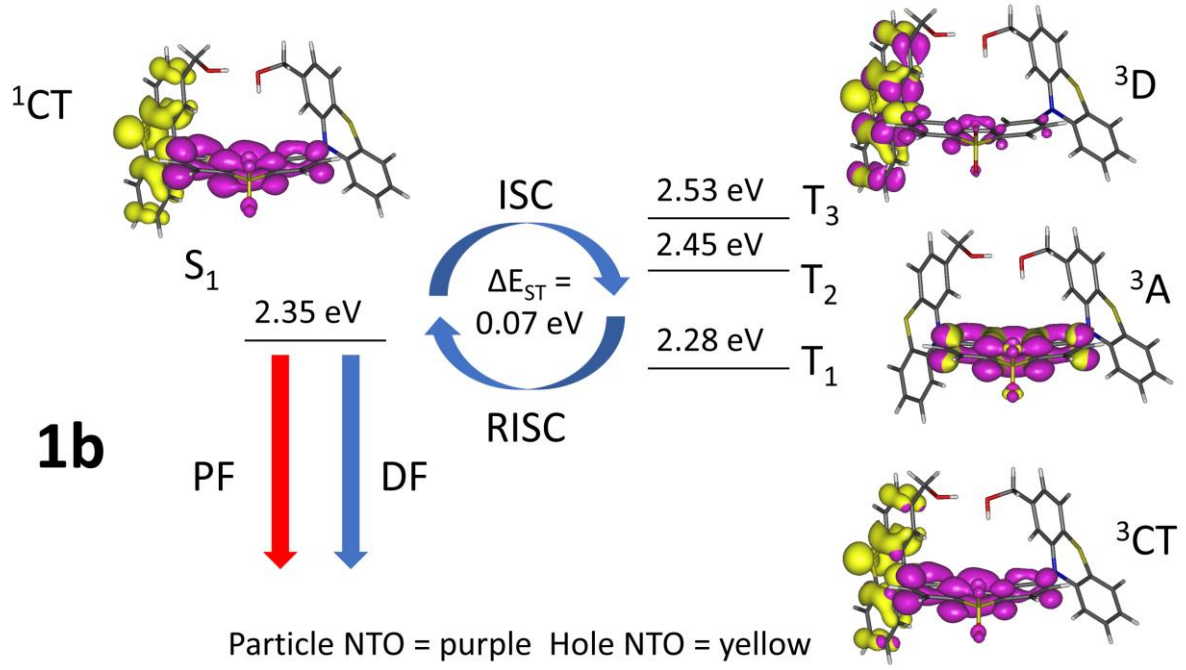

Figure 10. Energy diagram illustrating TADF with natural transition orbitals (NTOs) for each state on the optimized eq-eq S_1 excited state geometry for **1b** involving an intramolecular O–H...O interaction from TD-DFT computations. Contours in NTOs are drawn at ±0.04 $(e/bohr^3)^{1/2}$.

The ax-ax and ax-eq conformers optimized at the S_1 excited states of **1a–c** and **2a–c** were shown by TD-DFT computations to have large singlet-triplet gaps (ΔE_{ST}) at 0.27-1.30 eV (**Figures S56–57**, **Table S4**). These geometries do not contribute to the TADF processes in **1a-c** and **2a-c** but they may contribute to the prompt local fluorescence (^{1}LE) and local phosphorescence at room temperature observed in zeonex, where ax-ax and ax-eq conformers could be constrained after excitation to their excited states.

Conclusions

Efficient synthetic methodology has been developed to obtain cyclophanes **2a−c** which show TADF properties. Detailed photophysical and computational analysis shows that the cyclophane molecular architecture alters the conformational distribution of the phenothiazine donor units. Despite their different structures, **1a–c** and **2a–c** presented in this work have similar photophysical properties since they emit through similar excited states resulting from the presence of the equatorial conformation of their PTZ donor segments.

Due to the novel cyclophane structural design presented in this study, the axial arrangement of the PTZ units is suppressed, while a certain degree of rotational freedom of the intersegmental C–N axes, which is essential for efficient TADF, is retained. Despite the different polarity and rigidity of the linking elements, the basic photophysical properties and efficient TADF performance of the uncyclized parent compound **1a** can be preserved when linking the triad segments into a macrocycle.

The concept of building cyclophanes as TADF-active structures therefore offers multiple possibilities for controlling the intersegmental arrangement of donor–acceptor compounds. This is a valuable methodology for controlling the conformations of PTZ-based materials, and presents a synthetic platform for future work to introduce non-innocent functionality in close proximity to the TADF-active structure as part of the link between donor systems. In the present study the linker functionality does not significantly alter the excellent photophysical properties of the TADF systems and therefore the linker would be an ideal chemical position to tether the emitter for biological conjugation, sensing and other applications. This strategy offers an attractive avenue for using TADF-active structures as functional elements in more complex settings, i.e. TADF-emitting tags/labels, or future covalently bound hyperfluorescence systems.[49]

General Experimental Details

Solvents and reagents: Solvents were dried using an Innovative Technology solvent purification system and were stored in ampules under argon. Reagents were obtained from commercial sources and were used without further purification. Moisture and/or air sensitive experiments were conducted using thoroughly dried glassware under argon atmosphere.

NMR Spectra: ^{1}H-NMR spectra were recorded on Bruker AV400, Varian VNMRS 600 and 700 spectrometers operating at 400, 600 and 700 MHz, respectively. ^{13}C-NMR spectra were recorded on the same instruments at 100, 150 and 175 MHz respectively. Chemical shifts (δ) in ^{1}H-NMR and ^{13}C{^{1}H}-NMR spectra are reported in ppm and were referenced against the residual solvent signal as reported in the literature.[50]

Flash chromatography was carried out on silica gel 60 (40-63 μm) purchased from Fluorochem.

Mass spectra: High resolution mass spectrometry was carried out on a Waters LCT Premier XE using ASAP ionization with TOF detection. Samples were analyzed directly as solids.

Melting points were carried out on a Stuart SMP40 machine with a ramping rate of 4 °C min^{-1}. Videos were replayed manually to determine the melting point or melting range.

Cyclic voltammetry (CV) measurements were performed using a BAS CV50W electrochemical analyzer fitted with a three-electrode system consisting of a glassy carbon (ϕ = 3 mm) working electrode, and Pt wire counter and quasi reference electrodes. Experiments were conducted at a scan rate of 100 mV s^{-1}. All experiments were conducted in dry deoxygenated DMF with 0.1 M tetrabutylammonium hexafluorophosphate as the supporting electrolyte. All voltammograms presented were referenced using separate voltammograms with internal ferrocene (Fc = $(C_5H_5)_2Fe$). The HOMO and LUMO levels in **Table S1** were obtained from the onsets of the redox waves using the equations HOMO ~ ionization potential (IP) = $|e|(E_{ox(onset)}+5.1)$ eV and LUMO ~ electron affinity (EA) = (HOMO + E_g). The +5.1 V value is the ferrocene/ferrocenium couple potential, E_g representing the electrochemical potential difference between the first oxidation and reduction wave onsets.

Spectroscopic measurements in solution were carried out using dilute solutions with optical density ≈ 0.2 at the excitation wavelength. The solvents were super purity grade and used as supplied. Thin films in zeonex were prepared by drop casting with a guest:zeonex ratio of (1:20 *w/w*) from toluene solutions. Absorption and emission spectra were collected using a UV-3600 double beam spectrophotometer (Shimadzu) and a Fluorolog fluorescence spectrometer (Jobin Yvon). The extinction coefficient determination was performed in CH_2Cl_2 solution. Phosphorescence, prompt fluorescence (PF) and delayed fluorescence (DF) spectra and decays were recorded using nanosecond gated luminescence and lifetime measurements (from 800 ps to 1 s) with either a high energy pulsed Nd:YAG laser emitting at 355 nm (EKSPLA) or a N_2 laser emitting at 337 nm with pulse width 170 ps. Emission was focused onto a spectrograph and detected on a sensitive gated iCCD camera (Stanford Computer Optics) between 350 and 700 nm with sub-nanosecond resolution. Time-dependent spectroscopy measurements were performed by exponentially increasing the gate and delay times. The curve obtained directly from this process does not represent the real luminescence decay. However, this is easily corrected for by integrating the measured spectra and dividing the integral by the corresponding integration time. In this way, each experimental point represents a snapshot of the number of photons emitted per second at a time t = delay + (integration time)/2. The luminescence decay is then obtained by plotting each experimental point against time and fitting with the sum of exponentials. When required, in this way, we are able to collect luminescence decaying over 8 decades in time and in a single experiment, providing true kinetic data. For initial development and other applications of these methods; see literature studies.[12,13,51,52] PLQY measurements were obtained using quinine sulphate as the standard.[53]

Single-crystal X-ray diffraction experiments for **1c**, **2a-c** were carried out on a Bruker D8 Venture 3-circle diffractometer, equipped with PHOTON 100 CMOS area detector, using Mo-*K*α (**1c**, **2b**) or Cu-*K*α (**2a**, **2c**) radiation from Incoatec IμS microsources with focussing mirrors. The crystals were cooled using a Cryostream 700 open-flow N_2 gas cryostat (Oxford Cryosystems). The data were collected in shutterless mode by narrow frame ω scans covering full sphere of reciprocal space, using APEX3 v.2016.1-0 software, reflection intensities integrated using SAINT v. 8.37A or 8.38A software (Bruker AXS, 2016-2017). Data were corrected for absorption by semi-empirical method based on Laue equivalents and multiple scans (**1c**, **2b**) or by numerical integration based on crystal face-indexing (**2a**, **2c**), using SADABS software.[54] For **1b** the X-ray experiment was performed at Beamline I19 (EH1) of Diamond Light Source (RAL) on a dual air-bearing fixed-χ diffractometer with pixel-array photon-counting Dectris Pilatus 2M detector,[55] using undulator radiation monochromated with double-crystal Si(111). The crystal was cryo-mounted using remote-controlled BART robot [56] and cooled to 100 K using a Cryostream cryostat. Full sphere of reciprocal space was nominally covered by one run of 900 thin-slice φ-scans and 3 runs of 850 thin-slice ω-scans each (scan width 0.2°, 0.2 s exposure). The computations were carried out using Diamond I19 EH1 GDA[55] and DIALS software.[57] The diffraction images were merged pairwise and converted to Bruker format using cbf_to_sfrm.py program [56] and

further processed with APEX3 and SAINT software. The crystal was a 2-component twin, by a 176.8° rotation about the real axis [0.025 1 -0.032]. The diffraction pattern was deconvoluted using CELL_NOW v. 2008/4 program and integrated with two orientation matrices, yielding 108623 reflections (19944 unique) from the 1st domain, 108429 reflections (19965 unique) from the 2nd domain, and 1905 overlapping reflections (1046 unique) involving both domains. The data were scaled and merged by TWINABS program, which gave the domain ratio of 0.64:0.36. Alternatively, optimization of the domain contributions during structure refinement converged at 0.6515(7):0.3485(7).

Structure **2a** was solved by direct methods, using SHELXS 2013/1 program,[58] other structures by dual-space intrinsic phasing, using SHELXT 2018/2 program.[59] All structures were refined by full-matrix least squares using SHELXL software[60] on Olex2 platform.[61] Crystal data and other experimental details are listed in **Table S2**.

Geometry optimizations were carried out with the Gaussian 16 package.[62] Ground state (S_0) geometries were fully optimized from different starting geometries without symmetry constraints at B3LYP[63,64] with the 6-31(d) basis set.[65,66] All fully optimized S_0 geometries were found to be true minima based on no imaginary frequencies found and their Gibbs free energies determined from frequency calculations. The predicted absorption spectra were produced visually from 100 lowest singlet states determined by TD-DFT at B3LYP/6-31G(d). No oscillator strengths could be obtained for triplet state transitions within the TD-DFT setup.

The popular B3LYP functional (and indeed many other pure/hybrid density functional theory (DFT) methods with zero/low Hartree-Fock (HF) wave contributions) is known to significantly underestimate charge transfer (CT) energies with respect to local excitation (LE) energies.[67] Singlet excited state (S_1) geometries were optimized using the td opt command (TD-DFT) from fully optimized S_0 geometries as starting geometries at CAM-B3LYP/6-31G(d).[68] The larger HF contribution in CAM-B3LYP means that all computed transition energies are generally overestimated in time-dependent density functional theory (TD-DFT) calculations at CAM-B3LYP. The parameter μ in CAM-B3LYP determines the balance of DFT to HF exchange at the intermediate point in the long-range exchange interaction.[68] If $\mu = 0$, the long-range-corrected (LC) DFT calculation corresponds to the pure (non-LC) DFT calculation, and conversely $\mu = \infty$ corresponds to the standard HF calculation.[69] The parameter μ in CAM-B3LYP is 0.33 and, to lower the HF contribution, this parameter is adjusted to 0.27 for single point TD-DFT computations here and elsewhere for direct comparison with experimental emission data.[70-72] The CAM-B3LYP functional has been successfully applied to similar TADF molecules elsewhere.[73]

The six lowest singlet and six lowest triplet transitions were predicted from single point TD-DFT computations on the optimized S_1 geometries. Natural transition orbital (NTO) calculations were performed on the optimized S_1 geometries to visualize the hole and particle orbitals. The NTO figures

were generated using the Gabedit package.[74] The %CT values were derived by i) defining the atoms for donor and acceptor units, ii) calculating the %donor and %acceptor values in each molecular orbital using electronic structure calculations and iii) calculating the %CT from NTO orbitals using the single point TD-DFT generated data and the %donor and %acceptor values with GaussSum software.[75] Spin-orbit coupling matrix elements (SOCME) were obtained from TD-DFT computations at CAM-B3LYP with def2/J TZVP as basis set for the five lowest singlet and five lowest triplet transitions using the Orca package.[76]

Synthesis and Characterization

10*H*-Phenothiazine-2-carboxylic acid (4)

2-Cyanophenothiazine (5.33 g, 23.76 mmol, 1 eq.) was mixed with glacial acetic acid (140 mL) and conc. HCl (140 mL). The suspension was purged with argon for 15 minutes and was subsequently heated to 117 °C for 18 h using a dry block heater. The resulting brown mixture was cooled to room temperature and the solvent was removed under reduced pressure. The remaining residue was dissolved in ethyl acetate (150 mL) and was washed with H_2O (3 × 150 mL). The organic phase was dried using $MgSO_4$ and was filtered through a plug of silica. The solvent was removed under reduced pressure giving product as a yellow solid (5.58 g of **4**, ≈ 92% yield of **4**), which contained ≈ 5% starting material. The material was used in the next reaction step without further purification.

The analytical data is in agreement with the data reported in the literature.[77]

^{1}H-NMR (DMSO-d_6, 400 MHz, 300 K) δ (ppm) = 12.83 (s, 1H), 8.76 (s, 1H), 7.29 (dd, J = 7.9, 1.7 Hz, 1H), 7.24 (d, J = 1.7 Hz, 1H), 6.98–7.04 (m, 2H), 6.92 (dd, J = 7.7, 1.5 Hz, 1H), 6.77 (td, J = 7.5, 1.2 Hz, 1H), 6.66 (dd, J = 7.9, 1.2 Hz, 1H).

Methyl 10*H*-phenothiazine-2-carboxylate (5)

10*H*-Phenothiazine-2-carboxylic acid **4** (5.49 g, 22.57 mmol, 1 eq.) was suspended in acetone (80 mL). The mixture was purged with argon for 15 minutes, after which potassium carbonate (3.34 g, 24.82 mmol, 1.1 eq.) was added. After stirring the mixture for five minutes at room temperature, methyl iodide (1.83 mL/4.16 g, 29.34 mmol, 1.3 eq.) was added dropwise. The resulting mixture was stirred for 43 h at room temperature and was subsequently concentrated under reduced pressure. The resulting residue was mixed with water (100 mL) and was extracted with DCM (2 × 100 mL). The organic layer was dried over $MgSO_4$ and was filtered. Removal of solvent under reduced pressure gave product which was subsequently dissolve in *n*-hexane (20 mL). The mixture was filtered through a plug of silica and was concentrated under reduced pressure, giving the product as a yellow solid (4.08 g, 70%).

The analytical data is in agreement with those reported in the literature.[78]

^{1}H-NMR (DMSO-d_6, 400 MHz, 295 K) δ (ppm): 8.79 (s, 1H), 7.30 (dd, *J* = 8.0, 2.7 Hz, 1H), 7.25 (d, *J* = 1.8 Hz, 1H), 7.03 – 6.97 (m, 2H), 6.91 (dd, *J* = 7.7, 1.5 Hz, 1H), 6.77 (td, *J* = 7.5, 1.3 Hz, 1H), 6.65 (dd, *J* = 8.0, 1.2 Hz, 1H), 3.81 (s, 3H).

(10*H*-Phenothiazin-2-yl)methanol (6)

Under an argon atmosphere, to methyl 10*H*-phenothiazine-2-carboxylate **5** (3.10 g, 12.05 mmol, 1 eq.) was added dry Et_2O. (250 mL). In a separate flask, to $LiAlH_4$ (1.37 g, 36.14 mmol, 3 eq.) was added dry Et_2O (60 mL). The solution of **5** was slowly transferred to the $LiAlH_4$ mixture via cannula, and the resulting mixture was stirred for 4 h at room temperature. Carefully, 10% $HCl_{(aq.)}$ (30 mL) was added, and the resulting colorless solution was stirred for 20 min. The mixture was filtered through a plug of Celite™, dried using $MgSO_4$, filtered, and subsequently was concentrated under reduced pressure, giving product as a grey solid (2.13 g, 77%). The material was used without further purification.

This compound was previously reported in the literature.[79]

^{1}H-NMR (DMSO-d_6, 400 MHz, 296 K) δ (ppm): 8.57 (s, 1H), 6.99 (td, *J* = 7.6, 1.5 Hz, 1H), 6.91 (dd, *J* = 7.6, 1.4 Hz, 1H), 6.85 (d, *J* = 7.6 Hz, 1H), 6.75 (td, *J* = 7.5, 1.3 Hz, 1H), 6.72–6.66 (m, 3H), 5.15 (t, *J* = 5.7 Hz,1H), 4.35 (d, J = 5.7 Hz, 2H). m.p.: 204.3–206.0 °C.

2-(((*Tert*-butyldimethylsilyl)oxy)methyl)-10*H*-phenothiazine (7)

(10*H*-Phenothiazin-2-yl)methanol **6** (2.10 g, 9.16 mmol, 1 eq.) was suspended in anhydrous DCM (60 mL) under argon atmosphere and was mixed with imidazole (0.623 g, 9.16 mmol , 1 eq.), and *tert*-butyldimethylsilyl chloride (1.55 g, 10.28 mmol, 1.12 eq.). The mixture was stirred for 2.5 h at room temperature and was subsequently diluted with $NaCl_{(aq)}$ (100 mL). The resulting phases were separated, and the organic layer was dried using $MgSO_4$. The solution was filtered through a plug of silica. The solvent was removed under reduced pressure, yielding an off-white solid which was purified by column chromatography on silica (gradient *n*-Hexane/DCM, v/v, 5:1→3:1). The product was obtained as an off-white solid (3.08 g, 98%).

^{1}H-NMR (700 MHz, Acetone-d_6, 298 K) δ (ppm): 7.86 (s, 1H), 6.97 (t, *J* = 7.5 Hz, 1H), 6.93 (d, *J* = 7.5 Hz, 1H), 6.89 (d, *J* = 7.7 Hz, 1H), 6.80 – 6.74 (m, 3H), 6.70 (d, *J* = 7.9 Hz, 1H), 4.62 (s, 2H), 0.93 (s, 9H), 0.10 (s, 6H). ^{13}C{^{1}H}-NMR (176 MHz, Acetone-d_6, 298 K) δ (ppm): 143.4, 143.3, 142.3, 128.2, 127.2, 126.9, 122.8, 120.6, 118.5, 116.6, 115.4, 113.3, 65.1, 26.3, 18.9, –5.1. HRMS-ASAP-TOF$^+$ *m/z* calculated for $C_{19}H_{26}NOSSi$ $[MH]^+$ 344.1499, found: 344.1501. m.p. 169.5 – 171.0 °C

8

Under an argon atmosphere, the TBDMS-protected (10*H*-phenothiazin-2-yl)methanol **7** (2.84 g, 8.27 mmol, 2 eq.) was mixed with 2,8-dibromodibenzothiophene-*S*,*S*-dioxide[41] (1.55 g, 4.13 mmol, 1 eq.) and $HP^tBu_3BF_4$ (120 mg, 0.41 mmol, 0.10 eq.). The mixture was dissolved in dry toluene (100 mL) and the solution was bubbled with argon for 30 minutes. $Pd_2(dba)_3 \cdot CHCl_3$ (214 mg, 0.21 mmol, 0.05 eq.) was added and the mixture was bubbled with argon for 15 minutes. NaO^tBu (1.19 g, 12.40 mmol, 3.00 eq.) was then added and the mixture was heated to 107 °C using a dry block heater, with stirring for 21 h. The mixture was cooled to room temperature and filtered through plugs of Celite™ and silica. The solvent was removed under reduced pressure and the remaining residue was purified by column chromatography on silica (DCM/Hex, v/v, 7:3). Removal of solvent under reduced pressure gave the product was obtained as a yellow solid (2.83 g, 76%).

^{1}H-NMR (700 MHz, CD_2Cl_2, 298 K) δ (ppm): 7.74 (d, *J* = 8.4 Hz, 2H), 7.33 – 7.30 (m, 4H), 7.28 (dd, *J* = 8.4, 2.1 Hz, 2H), 7.26 (d, *J* = 7.9 Hz, 2H), 7.17 (td, *J* = 7.8, 1.5 Hz, 2H), 7.10 (td, *J* = 7.6, 1.1 Hz, 2H), 7.05 (d, *J* = 8.0 Hz, 2H), 6.96 – 6.93 (m, 4H), 4.63 (s, 4H), 0.84 (s, 18H), 0.02 (s, 12H). ^{13}C{^{1}H}-NMR (176 MHz, CD_2Cl_2, 298 K) δ (ppm): 149.4, 142.22, 142.16, 142.1, 134.1, 133.5, 129.5, 128.6, 128.3, 127.7, 127.4, 125.6, 123.8, 123.6, 123.2, 120.7, 114.2, 64.5, 26.0, 18.5, –5.2. Note: There is one less carbon signal than expected, ^{1}H-^{13}C HSQC NMR experiments show there are two different carbon environments overlapping with the same chemical shift at 123.2 ppm (**Figure S4**). HRMS-ASAP-TOF$^+$ m/z calculated for $C_{50}H_{54}N_2O_4Si_2S_3$ $[MH]^+$ 898.2779, found: 898.2780. m.p. 263.9–266.5 °C

1b

Under an argon atmosphere, TBDMS-protected compound **8** (3.27 g, 3.63 mmol, 1 eq.) was dissolved in dry THF (55 mL). To the yellow solution was added tetrabutylammonium fluoride in THF (7.26 mL, 1 M soln. in THF, 7.26 mmol, 2.00 eq.,) dropwise. The orange mixture was stirred for 4 h at room temperature and was subsequently added $NaCl_{(aq.)}$ sat. (50 mL). The mixture was diluted with EtOAc (50 mL) and the phases were separated, and the organic phase was dried using $MgSO_4$ which was subsequently filtered. The solvent was removed under reduced pressure and the remaining yellow solid was purified by column chromatography on silica, initially using DCM as mobile phase and subsequently eluting the target compound using a solvent mixture of *n*-hexane/acetone (v/v, 1:9). The residue of the combined fractions containing the desired product was triturated four times using boiling Et_2O. Removal of solvent under reduced pressure gave the product as an off-white solid (2.28 g, 94%). Note: There is one less carbon signal in the ^{13}C NMR than expected due to long relaxation times of quaternary carbons adjacent to nitrogen.

^{1}H-NMR (DMSO-d_6, 400 MHz, 294 K) δ (ppm): 7.98 (d, *J* = 8.45 Hz, 2H), 7.62 (s, 2H), 7.41 (d, *J* = 7.66 Hz, 2H), 7.36 (d, *J* = 7.90 Hz, 2H), 7.32 (d, *J* = 8.45 Hz, 2H), 7.26 (t, *J* = 7.78 Hz, 2H), 7.18 (t,

J = 7.47 Hz, 2H), 7.12 (d, *J* = 7.90 Hz, 2H), 7.07 (d, *J* = 7.96 Hz, 2H), 7.01 (s, 2H), 5.27 (t, *J* = 5.61 Hz, 2H), 4.43 (d, *J* = 5.16 Hz, 4H). $^{13}C\{^{1}H\}$-NMR (DMSO-d_6, 100 MHz, 294 K) δ (ppm) = 206.8, 148.8, 142.9, 141.4, 141.3, 133.0, 132.4, 128.2, 127.9, 127.9, 125.8, 125.6, 124.0, 123.6, 123.4, 123.3, 120.8, 114.3, 62.2. HRMS-ASAP-TOF$^+$ *m/z* calculated for $C_{38}H_{25}N_2O_3S_3$ $[M+H–H_2O]^+$ 653.1022, found: 653.1020. m.p. 295 °C (decomp.). Note: The benzylic alcohols in **1b** are prone to cleavage following protonation during the ASAP analysis. As a result the $[M+H^+]$ ion is very low in intensity and cannot be used for accurate mass. The ion resulting from water loss from **1b** following initial protonation dominates the signal and is within acceptable ppm ranges. The presence of both OH groups is confirmed by ^{1}H NMR and X-ray crystallography.

2a

To a solution of **1b** (117 mg, 0.174 mmol, 1 eq.) and isophthaloyl chloride (58 mg, 0.284 mmol, 1.64 eq.) in dry CH_2Cl_2 (275 mL) under argon was slowly added dry pyridine (0.28 mL, 3.48 mmol, 20 eq.). The reaction mixture was stirred at ambient temperature for 21.5 h. TLC analysis indicated complete conversion to product and the solvent was then removed under reduced pressure to yield a crude mixture. The crude mixture was purified by silica gel column chromatography with the following solvent mixtures: 20% acetone:hexane (*v/v*), 40% acetone: hexane, 100% CH_2Cl_2 and finally 1% acetone:CH_2Cl_2. Solvent was removed under reduced pressure to give compound **2a** as a yellow solid (87 mg, 62%). Crystals suitable for X-ray diffraction were grown by vapor diffusion of 2,2,4-trimethylpentane into a solution of **2a** in CH_2Cl_2.

^{1}H-NMR (400 MHz, DMSO-d_6, 295 K) δ (ppm): 8.31 (d, *J* = 8.2 Hz, 2H), 8.29 (d, *J* = 1.8 Hz, 2H), 8.19 (t, *J* = 1.6 Hz, 1H), 8.03 (dd, *J* = 7.8, 1.6 Hz, 2H), 7.75 (dd, *J* = 8.2, 1.8 Hz, 2H), 7.63 (t, *J* = 7.8 Hz, 1H), 7.11 (d, *J* = 7.9 Hz, 2H), 7.07 (dd, *J* = 7.4, 1.7 Hz, 2H), 6.96 (dd, *J* = 7.9, 1.5 Hz, 2H), 6.95 – 6.90 (m, 2H), 6.86 (td, *J* = 7.4, 1.3 Hz, 2H), 6.24 (dd, *J* = 8.2, 1.3 Hz, 2H), 6.11 (d, *J* = 1.5 Hz, 2H), 5.24 (s, 4H). $^{13}C\{^{1}H\}$-NMR (151 MHz, DMSO-d_6, 298 K) δ (ppm): 164.2, 146.1, 143.1, 142.0, 136.5, 136.0, 133.9, 133.8, 133.6, 130.1, 129.4, 129.0, 127.6, 126.7, 125.0, 124.7, 123.3, 122.7, 119.6, 119.4, 116.4, 114.8, 65.0. HRMS-ASAP-TOF$^+$ m/z calculated for $C_{46}H_{29}O_6S_3N_2$ $[MH]^+$ 801.1182, found: 801.1168. m.p. 328 °C (decomp.)

2b

Under an argon atmosphere, to sodium hydride (65 mg, 2.71 mmol, 6.06 eq.) as added anhydrous THF (200 mL) which was then heated to 65 °C. An anhydrous premixed solution of diol **1b** (300 mg, 0.45 mmol, 1 eq.) and α,α′-dibromo-*m*-xylene (118 mg, 0.45 mmol, 1 eq.) in THF (50 mL) was added dropwise over 48 h using a syringe pump. The reaction mixture was kept stirring at 65 °C for another 48 h using a dry block heater and was subsequently quenched by the addition of H_2O (10 mL). The solvent was removed under reduced pressure and the remaining residue was redissolved in DCM (50

mL) and $NaCl_{(aq)}$ sat. (50 mL). The organic phase was separated, dried using $MgSO_4$, and filtered through a plug of silica. The solvent was removed under reduced pressure a yellow solid which was recrystallized by dissolving in hot DCM, mixing with acetone and subsequently removing the DCM under elevated temperature. Combining the recrystallization crops resulted in pure product as a yellow solid (49 mg, 14%). Crystals suitable for X-ray diffraction were grown by dissolving the compound in DCM and overlaying the resulting solution with acetone. The DCM was subsequently allowed to evaporate over time.

^{1}H-NMR (CD_2Cl_2, 600 MHz, 298 K) δ (ppm): 7.98 (d, J = 8.2 Hz, 2H), 7.60 (s, J = 1.8 Hz, 2H), 7.51 (dt, J = 8.2, 1.8 Hz, 2H), 7.245 (t, J = 7.5 Hz, 1H), 7.09–7.17 (m, 7H), 6.98 (dt, J = 7.6, 1.6 Hz, 2H), 6.90–6.96 (m, 4H), 6.52 (dd, J = 8.1, 1.1 Hz, 2H), 6.39 (s, J = 1.3 Hz, 2H), 4.45 (s, 4H), 4.291 (s, 4H). ^{13}C{^{1}H}-NMR (CD_2Cl_2, 150 MHz, 298 K) δ (ppm): 148.1, 143.2, 142.9, 138.7, 138.6, 136.2, 134.2, 130.1, 128.7, 127.9, 127.7, 127.6, 127.5, 127.5, 124.9, 124.3, 124.2, 123.8, 123.4, 121.5, 119.1, 118.5, 72.7, 71.7. HRMS-ASAP-TOF$^+$ *m/z* calculated for $C_{46}H_{32}N_2O_4S_3$ $[M]^+$ 772.1524, found $[M]^+$ 772.1540. m.p. 320 °C (decomp.).

1c

Under an argon atmosphere, diol **1b** (700 mg, 1.04 mmol, 1 eq.) was mixed with anhydrous THF (20 mL) and sodium hydride (100 mg, 4.0 eq., 4.17 mmol). The mixture was stirred for 30 min at room temperature and subsequently allyl bromide (0.71 mL, 4.17 mmol, 4 eq.) was added. The mixture was heated to 60 °C for 20 h using a dry block heater and was cooled to room temperature. The reaction was quenched with ethanol (5 mL) and was concentrated under reduced pressure. The resulting residue was purified by column chromatography on silica, initially using DCM as mobile phase and subsequently eluting the material using pure THF. The product was obtained as a yellow solid (765 mg, 98%).

^{1}H-NMR (DMSO-d_6, 600 MHz, 298 K) δ (ppm) = 8.04 (d, J = 8.4 Hz, 2H), 7.77 (s, J = 2.0 Hz, 2H), 7.42 (d, J = 8.4, 2.0 Hz, 2H), 7.35 (d, J = 7.6, 1.5 Hz, 2H), 7.33 (d, J = 7.8 Hz, 2H), 7.21–7.17 (m, 2H), 7.12 (t, J = 7.6, 1.3 Hz, 2H), 7.067 (d, J = 8.0, 1.5 Hz, 2H), 6.92 (d, J = 8.1, 1.1 Hz, 2H), 6.85 (d, J = 1.3 Hz, 2H), 5.78 (m, 2H), 5.13 (dd, J = 17.3, 3.6 Hz, 2H), 5.01 (dd, J = 10.5, 3.3 Hz, 2H), 4.37 (s, 4H), 3.888 (m, 4H). ^{13}C{^{1}H}-NMR (DMSO-d_6, 150 MHz, 298 K) δ (ppm) = 148.1, 141.5, 141.5, 138.5, 134.9, 134.8, 133.2, 133.1, 127.9, 127.7, 126.4, 125.2, 125.2, 125.0, 124.1, 123.8, 121.8, 120.2, 116.4, 116.2, 116.2, 70.3, 70.2. HRMS-ASAP-TOF$^+$ *m/z* calculated for $C_{44}H_{34}N_2O_4S_3$ $[M]^+$ 750.1681, found $[M+H]^+$ 750.1683. m.p. 119–122°C.

2c

Under an argon atmosphere, bis-allyl substituted compound **1b** (308 mg, 0.41 mmol,1 eq.) was dissolved in DCM (260 mL) and was purged by argon bubbling for 30 min. In a separate flask, Grubbs-Hoveyda

2nd generation catalyst (15 mg, 0.024 mmol, 0.058 eq.) was dissolved in anhydrous DCM (10 mL). The solution of the catalyst was rapidly added to the solution of **1b** and the resulting mixture was stirred for 72 h at room temperature. A solution of potassium cyanoacetate (26 mg, 0.21 mmol, 0.51 eq.) in MeOH (2 mL) was added to the reaction and the resulting mixture was stirred for 30 min at room temperature. The solvent was removed under reduced pressure, and the resulting residue was purified by column chromatography on silica (toluene/EtOAc, v/v, 10:1). Removal of solvent under reduced pressure gave the product as a yellow solid (85 mg, 29%). Crystals suitable for X-ray crystallography were grown by dissolving **2c** in hot DMSO-d_6 and allowing cooling to ambient temperature.

^{1}H-NMR (DMSO-d_6, 700 MHz, 298 K) δ (ppm) = 8.48 (d, J = 1.8 Hz, 2H), 8.30 (d, J = 8.1 Hz, 2H), 7.68 (d, J = 8.1, 1.8 Hz, 2H), 7.01 (t, J = 7.8 Hz, 2H), 6.94 (t, J = 7.5 Hz, 2H), 6.88 (d, J = 7.9 Hz, 2H), 6.45 (d, J = 8.25 Hz, 2H), 6.30 (s, 2H), 5.55 (m, 2H), 4.21 (s, 4H), 3.85 (m, 4H). ^{13}C{^{1}H}-NMR (DMSO-d_6, 175 MHz, 294 K) δ (ppm) = 146.8, 142.7, 142.3, 138.2, 136.0, 133.4, 132.0, 128.9, 127.6, 126.9, 126.7, 125.2, 124.9, 123.4, 1228, 120.9, 120.0, 117.42 116.3, 70.3, 69.2. HRMS-ASAP-TOF$^+$ *m/z* calculated for $C_{42}H_{30}N_2O_4S_3$ $[M]^+$ 722.1368, found $[M]^+$ 722.1351. m.p. 288–290°C.

ASSOCIATED CONTENT

Supporting Information

The Supporting Information is available free of charge on the ACS Publications website at DOI: xxxxxxx.

^{1}H and ^{13}C{^{1}H} NMR spectra, additional photophysics, CV traces and data, and computational data (PDF)

Crystallographic information file for **1b-c** and **2a-c** (CIF)

Author Contributions

M.H., A.K.H., and J.S.W. all contributed equally to this manuscript. The manuscript was prepared and approved by all authors. The molecules presented were designed, synthesized, and characterized by M.H. and J.S.W. under the supervision of M.R.B. Electrochemistry was performed by M.H. with assistance from J.S.W. Photophysical measurements were performed by A.H. under the supervision of F.B.D. X-ray crystallography was performed by A.S.B. on crystals grown by M.H. and J.S.W. DFT calculations were performed and interpreted by M.A.F..

Acknowledgments

The authors thank EPRSC for funding grant code EP/L02621X/1. J.S.W. and M.R.B. thank EU Horizon 2020 grant agreement no. 732103 (HyperOLED) for funding. A.H. thanks EPSRC for the financial

support for a PhD grant. The Diamond Light Source is thanked for the award of instrument time on Station I19 (CY-22240) and the instrument scientists for their kind support.

References

(1) Kotha, S.; Shirbhate, M. E.; Waghule, G. T. Selected synthetic strategies to cyclophanes. *Beilstein J. Org. Chem.* **2015**, *11*, 1274-1331.

(2) Collins, M. S.; Carnes, M. E.; Nell, B. P.; Zakharov, L. N.; Johnson, D. W. A facile route to old and new cyclophanes via self-assembly and capture. *Nat. Commun.* **2016**, *7*, 11052.

(3) Barnes, J. C.; Juríček, M.; Vermeulen, N. A.; Dale, E. J.; Stoddart, J. F. Synthesis of ExnBox Cyclophanes. *J. Org. Chem.* **2013**, *78*, 11962-11969.

(4) Spenst, P.; Würthner, F. Photo- and redoxfunctional cyclophanes, macrocycles, and catenanes based on aromatic bisimides. *J. Photochem. Photobiol. C* **2017**, *31*, 114-138.

(5) Young, R. M.; Wasielewski, M. R. Mixed Electronic States in Molecular Dimers: Connecting Singlet Fission, Excimer Formation, and Symmetry-Breaking Charge Transfer. *Acc. Chem. Res.* **2020**, *53*, 1957-1968.

(6) Amabilino, D. B.; Dietrich-Buchecker, C. O.; Livoreil, A.; Pérez-García, L.; Sauvage, J.-P.; Stoddart, J. F. A Switchable Hybrid [2]-Catenane Based on Transition Metal Complexation and π-Electron Donor−Acceptor Interactions. *J. Am. Chem. Soc.* **1996**, *118*, 3905-3913.

(7) Livoreil, A.; Dietrich-Buchecker, C. O.; Sauvage, J.-P. Electrochemically Triggered Swinging of a [2]-Catenate. *J. Am. Chem. Soc.* **1994**, *116*, 9399-9400.

(8) Xue, M.; Yang, Y.; Chi, X.; Yan, X.; Huang, F. Development of Pseudorotaxanes and Rotaxanes: From Synthesis to Stimuli-Responsive Motions to Applications. *Chem. Rev.* **2015**, *115*, 7398-7501.

(9) Bissell, R. A.; Córdova, E.; Kaifer, A. E.; Stoddart, J. F. A chemically and electrochemically switchable molecular shuttle. *Nature* **1994**, *369*, 133-137.

(10) Badjić, J. D.; Balzani, V.; Credi, A.; Silvi, S.; Stoddart, J. F. A Molecular Elevator. *Science* **2004**, *303*, 1845.

(11) Stoddart, J. F. Mechanically Interlocked Molecules (MIMs)—Molecular Shuttles, Switches, and Machines (Nobel Lecture). *Angew. Chem. Int. Ed.* **2017**, *56*, 11094-11125.

(12) Ward, J. S.; Nobuyasu, R. S.; Fox, M. A.; Batsanov, A. S.; Santos, J.; Dias, F. B.; Bryce, M. R. Bond rotations and heteroatom effects in donor-acceptor-donor molecules: Implications for thermally activated delayed fluorescence and room temperature phosphorescence. *J. Org. Chem.* **2018**, *83*, 14431-14442.

(13) Ward, J. S.; Nobuyasu, R. S.; Fox, M. A.; Aguilar, J. A.; Hall, D.; Batsanov, A. S.; Ren, Z.; Dias, F. B.; Bryce, M. R. Impact of Methoxy Substituents on Thermally Activated Delayed Fluorescence and Room-Temperature Phosphorescence in All-Organic Donor-Acceptor Systems. *J. Org. Chem.* **2019**, *84*, 3801-3816.

(14) Izumi, S.; Higginbotham, H. F.; Nyga, A.; Stachelek, P.; Tohnai, N.; Silva, P.; Data, P.; Takeda, Y.; Minakata, S. Thermally Activated Delayed Fluorescent Donor–Acceptor–Donor–Acceptor π-Conjugated Macrocycle for Organic Light-Emitting Diodes. *J. Am. Chem. Soc.* **2020**, *142*, 1482-1491.

(15) Wong, M. Y.; Zysman-Colman, E. Purely Organic Thermally Activated Delayed Fluorescence Materials for Organic Light-Emitting Diodes. *Adv. Mater.* **2017**, *29*, 1605444.

(16) Yang, Z.; Mao, Z.; Xie, Z.; Zhang, Y.; Liu, S.; Zhao, J.; Xu, J.; Chi, Z.; Aldred, M. P. Recent advances in organic thermally activated delayed fluorescence materials. *Chem. Soc. Rev.* **2017**, *46*, 915-1016.

(17) Liu, Y. C.; Li, C. S.; Ren, Z. J.; Yan, S. K.; Bryce, M. R. All-organic thermally activated delayed fluorescence materials for organic light-emitting diodes. *Nat. Rev. Mater.* **2018**, *3*, 18020.

(18) Kim, J. U.; Park, I. S.; Chan, C.-Y.; Tanaka, M.; Tsuchiya, Y.; Nakanotani, H.; Adachi, C. Nanosecond-time-scale delayed fluorescence molecule for deep-blue OLEDs with small efficiency rolloff. *Nat. Commun.* **2020**, *11*, 1765.

(19) Yin, C.; Zhang, D.; Duan, L. A perspective on blue TADF materials based on carbazole-benzonitrile derivatives for efficient and stable OLEDs. *Appl. Phys. Lett.* **2020**, *116*, 120503.

(20) Wex, B.; Kaafarani, B. R. Perspective on carbazole-based organic compounds as emitters and hosts in TADF applications. *J. Mater. Chem. C* **2017**, *5*, 8622-8653.

(21) Sun, J. W.; Baek, J. Y.; Kim, K.-H.; Huh, J.-S.; Kwon, S.-K.; Kim, Y.-H.; Kim, J.-J. Azasiline-based thermally activated delayed fluorescence emitters for blue organic light emitting diodes. *J. Mater. Chem. C* **2017**, *5*, 1027-1032.

(22) Dias, F. B.; Bourdakos, K. N.; Jankus, V.; Moss, K. C.; Kamtekar, K. T.; Bhalla, V.; Santos, J.; Bryce, M. R.; Monkman, A. P. Triplet Harvesting with 100% Efficiency by Way of Thermally Activated Delayed Fluorescence in Charge Transfer OLED Emitters. *Adv. Mat.* **2013**, *25*, 3707-3714.

(23) Uoyama, H.; Goushi, K.; Shizu, K.; Nomura, H.; Adachi, C. Highly efficient organic light-emitting diodes from delayed fluorescence. *Nature* **2012**, *492*, 234-238.

(24) Duan, J.; Liu, D.; Tian, W.; Jiang, L.; Jiang, W.; Sun, Y. Elevating the triplet level of carbazolyl benzonitrile-based dendritic hosts by suppressing intramolecular charge transfer for solution-processed blue thermally activated delayed fluorescence OLEDs. *Opt. Mater.* **2020**, *104*, 109941.

(25) Zhang, Q. S.; Li, B.; Huang, S. P.; Nomura, H.; Tanaka, H.; Adachi, C. Efficient blue organic light-emitting diodes employing thermally activated delayed fluorescence. *Nat. Photonics* **2014**, *8*, 326-332.

(26) Kumar, S.; Ma, Y.-Y.; Khan, A.; Yuan, Y.; Yang, S.-Y.; Jiang, Z.-Q.; Fung, M.-K.; Liao, L.-S. Structurally controlled singlet-triplet splitting for blue star-shaped thermally activated delayed fluorescence emitters incorporating the tricarbazoles-triazine motifs. *Org. Electron.* **2020**, *84*, 105783.

(27) Zhang, Y. W.; Zhang, D. D.; Wei, J. B.; Liu, Z. Y.; Lu, Y.; Duan, L. Multi-Resonance Induced Thermally Activated Delayed Fluorophores for Narrowband Green OLEDs. *Angew. Chem. Int. Ed.* **2019**, *58*, 16912-16917.

(28) Yuan, W. B.; Zhang, M. C.; Zhang, X. P.; Cao, X. D.; Sun, N.; Wan, S. G.; Tao, Y. T. The electron inductive effect of CF3 on penta-carbazole containing blue emitters: Trade-off between color purity and luminescent efficiency in TADF OLEDs. *Dyes Pigm.* **2018**, *159*, 151-157.

(29) Geng, Y.; D'Aleo, A.; Inada, K.; Cui, L. S.; Kim, J. U.; Nakanotani, H.; Adachi, C. Donor-σ-Acceptor Motifs: Thermally Activated Delayed Fluorescence Emitters with Dual Upconversion. *Angew. Chem. Int. Ed.* **2017**, *56*, 16536-16540.

(30) Sauvé, E. R.; Paeng, J.; Yamaguchi, S.; Hudson, Z. M. Donor–Acceptor Materials Exhibiting Thermally Activated Delayed Fluorescence Using a Planarized N-Phenylbenzimidazole Acceptor. *J. Org. Chem.* **2020**, *85*, 108-117.

(31) Etherington, M. K.; Gibson, J.; Higginbotham, H. F.; Penfold, T. J.; Monkman, A. P. Revealing the spin–vibronic coupling mechanism of thermally activated delayed fluorescence. *Nat. Commun.* **2016**, *7*, 13680.

(32) Dias, F. B.; Santos, J.; Graves, D. R.; Data, P.; Nobuyasu, R. S.; Fox, M. A.; Batsanov, A. S.; Palmeira, T.; Berberan-Santos, M. N.; Bryce, M. R.; Monkman, A. P. The Role of Local Triplet Excited States and D-A Relative Orientation in Thermally Activated Delayed Fluorescence: Photophysics and Devices. *Adv. Sci.* **2016**, *3*, 1600080.

(33) Chen, X.-K.; Kim, D.; Brédas, J.-L. Thermally Activated Delayed Fluorescence (TADF) Path toward Efficient Electroluminescence in Purely Organic Materials: Molecular Level Insight. *Acc. Chem. Res.* **2018**, *51*, 2215-2224.

(34) Ward, J. S.; Kukhta, N. A.; dos Santos, P. L.; Congrave, D. G.; Batsanov, A. S.; Monkman, A. P.; Bryce, M. R. Delayed Blue Fluorescence via Upper-Triplet State Crossing from C–C Bonded Donor–Acceptor Charge Transfer Molecules with Azatriangulene Cores. *Chem. Mater.* **2019**, *31*, 6684-6695.

(35) Nobuyasu, R. S.; Ward, J. S.; Gibson, J.; Laidlaw, B. A.; Ren, Z. J.; Data, P.; Batsanov, A. S.; Penfold, T. J.; Bryce, M. R.; Dias, F. B. The influence of molecular geometry on the efficiency of thermally activated delayed fluorescence. *J. Mater. Chem. C* **2019**, *7*, 6672-6684.

(36) Etherington, M. K.; Franchello, F.; Gibson, J.; Northey, T.; Santos, J.; Ward, J. S.; Higginbotham, H. F.; Data, P.; Kurowska, A.; Dos Santos, P. L.; Graves, D. R.; Batsanov, A. S.; Dias, F. B.; Bryce, M. R.; Penfold, T. J.; Monkman, A. P. Regio- and conformational isomerization critical to design of efficient thermally-activated delayed fluorescence emitters. *Nat. Commun.* **2017**, *8*, 14987.

(37) Li, B.; Li, Z.; Guo, F.; Song, J.; Jiang, X.; Wang, Y.; Gao, S.; Wang, J.; Pang, X.; Zhao, L.; Zhang, Y. Realizing Efficient Single Organic Molecular White Light-Emitting Diodes from Conformational Isomerization of Quinazoline-Based Emitters. *ACS Appl. Mater. Interfaces* **2020**, *12*, 14233-14243.

(38) Okazaki, M.; Takeda, Y.; Data, P.; Pander, P.; Higginbotham, H.; Monkman, A. P.; Minakata, S. Thermally activated delayed fluorescent phenothiazine–dibenzo[a,j]phenazine–phenothiazine triads exhibiting tricolor-changing mechanochromic luminescence. *Chem. Sci.* **2017**, *8*, 2677-2686.

(39) Chen, D. G.; Lin, T. C.; Chen, Y. A.; Chen, Y. H.; Lin, T. C.; Chen, Y. T.; Chou, P. T. Revisiting Dual Intramolecular Charge-Transfer Fluorescence of Phenothiazine-triphenyltriazine Derivatives. *J. Phys. Chem. C* **2018**, *122*, 12215-12221.

(40) Stockmann, A.; Kurzawa, J.; Fritz, N.; Acar, N.; Schneider, S.; Daub, J.; Engl, R.; Clark, T. Conformational Control of Photoinduced Charge Separation within Phenothiazine−Pyrene Dyads. *J. Phys. Chem. A* **2002**, *106*, 7958-7970.

(41) Ward, J. S.; Nobuyasu, R. S.; Batsanov, A. S.; Data, P.; Monkman, A. P.; Dias, F. B.; Bryce, M. R. The interplay of thermally activated delayed fluorescence (TADF) and room temperature organic phosphorescence in sterically-constrained donor-acceptor charge-transfer molecules. *Chem. Commun.* **2016**, *52*, 2612-2615.

(42) Hu, Y.; Wang, Z.; Jiang, X.; Cai, X.; Su, S.-J.; Huang, F.; Cao, Y. One-step synthesis of cyclic compounds towards easy room-temperature phosphorescence and deep blue thermally activated delayed fluorescence. *Chem. Commun.* **2018**, *54*, 7850-7853.

(43) Spuling, E.; Sharma, N.; Samuel, I. D. W.; Zysman-Colman, E.; Bräse, S. (Deep) blue through-space conjugated TADF emitters based on [2.2]paracyclophanes. *Chem. Commun.* **2018**, *54*, 9278-9281.

(44) Kawasumi, K.; Wu, T.; Zhu, T.; Chae, H. S.; Van Voorhis, T.; Baldo, M. A.; Swager, T. M. Thermally Activated Delayed Fluorescence Materials Based on Homoconjugation Effect of Donor–Acceptor Triptycenes. *J. Am. Chem. Soc.* **2015**, *137*, 11908-11911.

(45) Sharma, N.; Spuling, E.; Mattern, Cornelia M.; Li, W.; Fuhr, O.; Tsuchiya, Y.; Adachi, C.; Bräse, S.; Samuel, I. D. W.; Zysman-Colman, E. Turn on of sky-blue thermally activated delayed fluorescence and circularly polarized luminescence (CPL) via increased torsion by a bulky carbazolophane donor. *Chem. Sci.* **2019**, *10*, 6689-6696.

(46) Etter, M. C. Encoding and decoding hydrogen-bond patterns of organic compounds. *Acc. Chem. Res.* **1990**, *23*, 120-126.

(47) Mayer, L.; May, L.; Müller, T. J. J. The interplay of conformations and electronic properties in *N*-aryl phenothiazines. *Org. Chem. Front.* **2020**, *7*, 1206-1217.

(48) Zhang, Z.; Gao, Y.; Liu, H.; Bai, Q.; Li, J. Y.; Liu, L. Q.; Wu, C. F.; Yang, B.; Wang, K.; Zou, B.; Wang, Y.; Lu, P. Dual fluorescence polymorphs: Wide-range emission from blue to red regulated by TICT and their dynamic electron state behavior under external pressure. *Dyes Pigm.* **2017**, *145*, 294-300.

(49) Nakanotani, H.; Higuchi, T.; Furukawa, T.; Masui, K.; Morimoto, K.; Numata, M.; Tanaka, H.; Sagara, Y.; Yasuda, T.; Adachi, C. High-efficiency organic light-emitting diodes with fluorescent emitters. *Nat. Commun.* **2014**, *5*, 4016.

(50) Fulmer, G. R.; Miller, A. J. M.; Sherden, N. H.; Gottlieb, H. E.; Nudelman, A.; Stoltz, B. M.; Bercaw, J. E.; Goldberg, K. I. NMR Chemical Shifts of Trace Impurities: Common Laboratory Solvents, Organics, and Gases in Deuterated Solvents Relevant to the Organometallic Chemist. *Organometallics* **2010**, *29*, 2176-2179.

(51) Rothe, C.; Monkman, A. P. Triplet exciton migration in a conjugated polyfluorene. *Phys. Rev. B* **2003**, *68*, 075208.

(52) Pander, P.; Data, P.; Dias, F. B. Time-resolved Photophysical Characterization of Triplet-harvesting Organic Compounds at an Oxygen-free Environment Using an iCCD Camera. *J. Vis. Exp.* **2018**, e56614.

(53) Williams, A. T. R.; Winfield, S. A.; Miller, J. N. Relative fluorescence quantum yields using a computer-controlled luminescence spectrometer. *Analyst* **1983**, *108*, 1067-1071.

(54) Krause, L.; Herbst-Irmer, R.; Sheldrick, G. M.; Stalke, D. Comparison of silver and molybdenum microfocus X-ray sources for single-crystal structure determination. *J. Appl. Crystallogr.* **2015**, *48*, 3-10.

(55) Allan, R. D.; Nowell, H.; Barnett, A. S.; Warren, R. M.; Wilcox, A.; Christensen, J.; Saunders, K. L.; Peach, A.; Hooper, T. M.; Zaja, L.; Patel, S.; Cahill, L.; Marshall, R.; Trimnell, S.; Foster, J. A.; Bates, T.; Lay, S.; Williams, A. M.; Hathaway, V. P.; Winter, G.; Gerstel, M.; Wooley, W. R. A Novel Dual Air-Bearing Fixed-χ Diffractometer for Small-Molecule Single-Crystal X-ray Diffraction on Beamline I19 at Diamond Light Source. *Crystals* **2017**, *7*, 336.

(56) Johnson, T. N.; Waddell, G. P.; Clegg, W.; Probert, R. M. Remote Access Revolution: Chemical Crystallographers Enter a New Era at Diamond Light Source Beamline I19. *Crystals* **2017**, *7*, 360.

(57) Winter, G.; Waterman, D. G.; Parkhurst, J. M.; Brewster, A. S.; Gildea, R. J.; Gerstel, M.; Fuentes-Montero, L.; Vollmar, M.; Michels-Clark, T.; Young, I. D.; Sauter, N. K.; Evans, G. DIALS: implementation and evaluation of a new integration package. *Acta Crystallogr D Struct Biol* **2018**, *74*, 85-97.

(58) Sheldrick, G. M. A short history of SHELX. *Acta Crystallogr. A* **2008**, *64*, 112-122.

(59) Sheldrick, G. M. SHELXT - integrated space-group and crystal-structure determination. *Acta Crystallogr. A* **2015**, *71*, 3-8.

(60) Sheldrick, G. M. Crystal structure refinement with SHELXL. *Acta Crystallogr. C Struct. Chem.* **2015**, *71*, 3-8.

(61) Dolomanov, O. V.; Bourhis, L. J.; Gildea, R. J.; Howard, J. A. K.; Puschmann, H. OLEX2: a complete structure solution, refinement and analysis program. *J. Appl. Crystallogr.* **2009**, *42*, 339-341.

(62) Frisch, M. J.; Trucks, G. W.; Schlegel, H. B.; Scuseria, G. E.; Robb, M. A.; Cheeseman, J. R.; Scalmani, G.; Barone, V.; Petersson, G. A.; Nakatsuji, H.; Li, X.; Caricato, M.; Marenich, A. V.; Bloino, J.; Janesko, B. G.; Gomperts, R.; Mennucci, B.; Hratchian, H. P.; Ortiz, J. V.; Izmaylov, A. F.; Sonnenberg, J. L.; Williams; Ding, F.; Lipparini, F.; Egidi, F.; Goings, J.; Peng, B.; Petrone, A.; Henderson, T.; Ranasinghe, D.; Zakrzewski, V. G.; Gao, J.; Rega, N.; Zheng, G.; Liang, W.; Hada, M.; Ehara, M.; Toyota, K.; Fukuda, R.; Hasegawa, J.; Ishida, M.; Nakajima, T.; Honda, Y.; Kitao, O.; Nakai, H.; Vreven, T.; Throssell, K.; Montgomery Jr., J. A.; Peralta, J. E.; Ogliaro, F.; Bearpark, M. J.; Heyd, J. J.; Brothers, E. N.; Kudin, K. N.; Staroverov, V. N.; Keith, T. A.; Kobayashi, R.; Normand, J.; Raghavachari, K.; Rendell, A. P.; Burant, J. C.; Iyengar, S. S.; Tomasi, J.; Cossi, M.; Millam, J. M.; Klene, M.; Adamo, C.; Cammi, R.; Ochterski, J. W.; Martin, R. L.; Morokuma, K.; Farkas, O.; Foresman, J. B.; Fox, D. J. *Gaussian 16, Revision B.01,* 2016.

(63) Becke, A. D. Density-Functional Thermochemistry. III. The Role of Exact Exchange. *J. Chem. Phys.* **1993**, *98*, 5648-5652.

(64) Lee, C. T.; Yang, W. T.; Parr, R. G. Development of the Colle-Salvetti Correlation-Energy Formula into a Functional of the Electron-Density. *Phys. Rev. B* **1988**, *37*, 785-789.

(65) Petersson, G. A.; Bennett, A.; Tensfeldt, T. G.; Allaham, M. A.; Shirley, W. A.; Mantzaris, J. A Complete Basis Set Model Chemistry. I. The Total Energies of Closed-Shell Atoms and Hydrides of the 1st-Row Elements. *J. Chem. Phys.* **1988**, *89*, 2193-2218.

(66) Petersson, G. A.; Allaham, M. A. A Complete Basis Set Model Chemistry. II. Open-Shell Systems and the Total Energies of the 1st-Row Atoms. *J. Chem. Phys.* **1991**, *94*, 6081-6090.

(67) Dreuw, A.; Weisman, J. L.; Head-Gordon, M. Long-range charge-transfer excited states in time-dependent density functional theory require non-local exchange. *J. Chem. Phys.* **2003**, *119*, 2943-2946.

(68) Yanai, T.; Tew, D. P.; Handy, N. C. A new hybrid exchange-correlation functional using the Coulomb-attenuating method (CAM-B3LYP). *Chem. Phys. Lett.* **2004**, *393*, 51-57.

(69) Tawada, Y.; Tsuneda, T.; Yanagisawa, S.; Yanai, T.; Hirao, K. A long-range-corrected time-dependent density functional theory. *J. Chem. Phys.* **2004**, *120*, 8425-8433.

(70) Peach, M. J. G.; Cohen, A. J.; Tozer, D. J. Influence of Coulomb-attenuation on exchange–correlation functional quality. *Phys. Chem. Chem. Phys* **2006**, *8*, 4543-4549.

(71) Mandal, I.; Manna, S.; Venkatramani, R. UV–Visible Lysine–Glutamate Dimer Excitations in Protein Charge Transfer Spectra: TDDFT Descriptions Using an Optimally Tuned CAM-B3LYP Functional. *J. Phys. Chem. B.* **2019**, *123*, 10967-10979.

(72) Ward, J. S.; Danos, A.; Stachelek, P.; Fox, M. A.; Batsanov, A. S.; Monkman, A. P.; Bryce, M. R. Exploiting Trifluoromethyl Substituents for Tuning Orbital Character of Singlet and Triplet States to Increase the Rate of Thermally Activated Delayed Fluorescence. *Mater. Chem. Front.* **2020**, DOI: 10.1039/d1030qm00429d.

(73) Samanta, P. K.; Kim, D.; Coropceanu, V.; Bredas, J. L. Up-Conversion Intersystem Crossing Rates in Organic Emitters for Thermally Activated Delayed Fluorescence: Impact of the Nature of Singlet vs Triplet Excited States. *J. Am. Chem. Soc.* **2017**, *139*, 4042-4051.

(74) Allouche, A. R. Gabedit-A Graphical User Interface for Computational Chemistry Softwares. *J. Comput. Chem.* **2011**, *32*, 174-182.

(75) O'Boyle, N. M.; Tenderholt, A. L.; Langner, K. M. cclib: A library for package-independent computational chemistry algorithms. *J. Comput. Chem.* **2008**, *29*, 839-845.

(76) Neese, F.; Aravena, D.; Atanasov, M.; Auer, A. A.; Becker, U.; Bistoni, G.; Brehm, M.; Bykov, D.; Chilkuri, V. G.; Datta, D.; Dutta, A. K.; Ganyushin, D.; Garcia, M.; Guo, Y.; Hansen, A.; Helmich-Paris, B.; Huntington, L.; Izsak, R.; Kollmar, C.; Kossmann, S.; Krupicka, M.; Lang, L.; Lenk, D.; Liakos, D.; Manganas, D.; Pantazis, D.; Petrenko, T.; Pinski, P.; Reimann, C.; Retegan, M.; Riplinger, C.; Risthaus, T.; Roemelt, M.; Saitow, M.; Sandhofer, B.; Sen, A.; Sivalingam, K.; Souza, B.; Stoychev, G.; Van den Heuvel, W.; Wezisla , B.; Wennmohs, F. *Orca Version 4.1.1*, 2019.

(77) Chitta Das, T.; Quadri, S. A.; Jadav, S. L.; Farooqui, M. Synthesis of new 2-substituted-10-phenylsulfonylphenothiazine conjugates and evaluation as anticancer agents by investigating their off-target mechanism. *Chem. Biol. Interface* **2018**, *8*, 84-93.

(78) Zhou, Y.; Zeng, Q.; Zhang, L. Transition-metal-free synthesis of phenothiazines from S-2-acetamidophenyl ethanethioate and ortho-dihaloarenes. *Synth. Commun.* **2017**, *47*, 710-715.

(79) Burger, A.; Clements, J. B. SOME DERIVATIVES OF PHENOTHIAZINE. *J. Org. Chem.* **1954**, *19*, 1113-1116.

(For Table of Contents Only)

TADF Emitting Materials

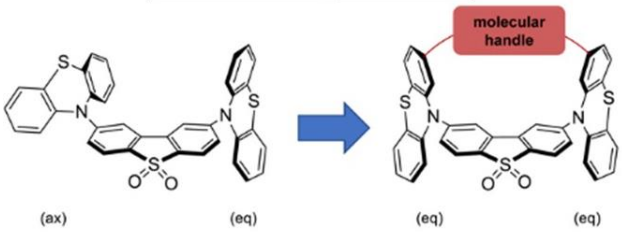

- **Controlling donor conformation/intersegmental dynamics**
- **Adding molecular functionality**